

SECOND ANNUAL REPORT

NASA Research Grant NAG3-1384

Period of Performance

11/18/93 through 11/18/94

**DYNAMICS AND STATICS
OF
NONAXISYMMETRIC LIQUID BRIDGES**

PREPARED BY:

**J. IWAN D. ALEXANDER
(Principal Investigator)**

ANDY RESNICK

YIQIANG ZHANG

A. FEDOSEYEV

**Center for Microgravity and Materials Research
The University of Alabama in Huntsville
Huntsville, Alabama 35899**

DYNAMICS AND STATICS OF NONAXISYMMETRIC LIQUID BRIDGES

NAG3-1384 Second Annual Report

Period of Performance 11/18/93 - 11/18/94

1. GENERAL

During second year we finished the construction of the experimental apparatus, and the design and testing of some of the visualization and data acquisition techniques. Experimental work focused on three areas: force measurements, loss of stability to nonaxisymmetric bridges, and vibration behavior. The experimental work is summarized in section 2. Selected results from our force measurement experiments are outlined in 3. In addition we worked on the theory of the dynamic stability of axisymmetric bridges and undertook numerical simulation of the effects of inclined gravity vectors on the minimum volume stability limit for static bridges. The results and status of our theoretical work and numerical simulation are described in sections 4.

Papers published and in preparation, conference presentations, etc., are described in section 5. Work planned for the third year is discussed in section 6. References cited in the report are listed in section 7.

2. EXPERIMENTAL WORK

Experiments have been carried out in three areas.

- a) Stability limits, symmetric and nonsymmetric breaking behavior of initially axisymmetric bridges.
- b) Lateral shearing, squeezing and force measurements.
- c) Vibration dynamics and breaking behavior.

The experimental set-up was completed early during the second year and is described in our earlier reports. Experiments are conducted in a neutral-buoyancy or Plateau tank. The bridges are held between rigid supports that allow for rotation and lateral and vertical translation. Each support can be independently vibrated at frequencies less than 10 Hz. Bridge injection is automated with simultaneous recording of precise volume and aspect ratio data. We use two imaging methods. Video images are obtained from two orthogonal cameras. In addition, a high quality Fourier transform imaging system for edge detection is being developed and the basic system assembled is now ready.

Preliminary experimental results concerning vibration and breakage were described in the third semi-annual report. This work is not yet complete. The bulk of our experimental work completed since then involves force measurements and is described below.

3. FORCE MEASUREMENTS ON LIQUID BRIDGES

3.1 Introduction

Forces exerted by a liquid bridge on a solid support are important in a variety of physical systems [1-5] including powder wetting, deformation of porous or unconsolidated media, crystal growth and in adhesion problems. The forces involved are due to the surface tension exerted by the meniscus, the pressure difference between the bridge and the surrounding medium (supported by the curvature of the surface) and the buoyancy force associated with the wetted portions of the supports. For a liquid bridge held between two flat coaxial equidimensional circular disks, we used a force deflection apparatus to measure the total force exerted by a liquid bridge on the lower disk. The lower disk is attached to the end of a long cantilever arm. The cantilever arm acts as a weak spring. The liquid bridge displaces the disk by an amount proportional to the total force, \tilde{F} , exerted on the disk. Then, by directly measuring the displacement, we can determine \tilde{F} . After calibrating the deflection of the cantilever arm with known applied loads, two sets of experiments were performed. In the first set, the total force was measured for various aspect ratio right circular cylindrical bridges. It is easy to calculate the forces exerted by right circular cylindrical bridges, and to verify the measurement by comparison with theoretical predictions. We can directly measure the interfacial energy at low Bond numbers, which we have previously been unable to do. The second set of experiments involves measuring the force exerted by liquid bridges with a variety of aspect ratios and volumes at different Bond numbers. The principal question to be answered here is how the combined capillary and pressure forces vary with bridge volume and aspect ratio.

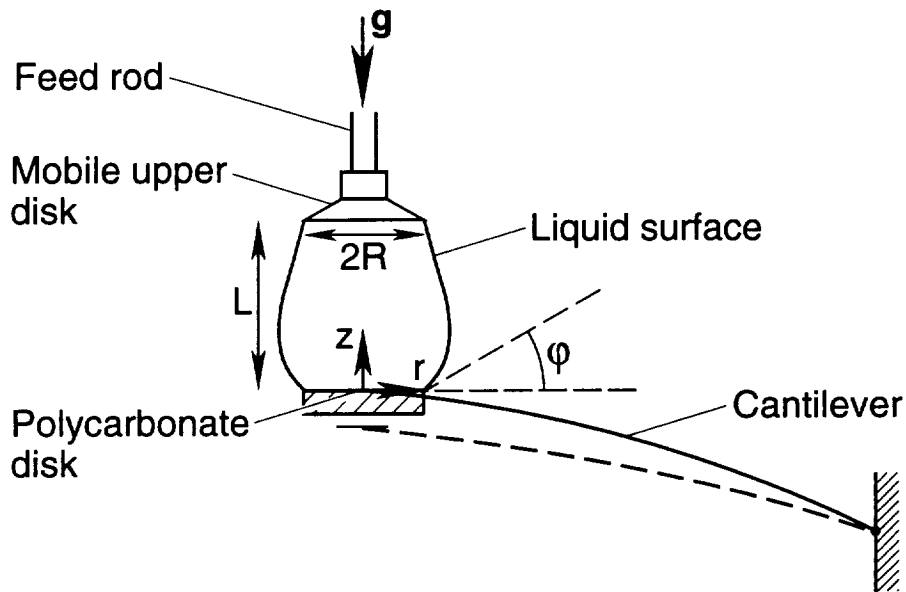


Fig. 1 Experimental set-up for force measurements

3.1.1 Theory

Consider a liquid bridge held between two equidimensional coaxial disks of radius R immersed in a liquid bath of density ρ_b (see Fig. 1). The total force \tilde{F} exerted on the lower disk [3, 6-8] consists of the capillary pressure \tilde{F}_{CP} and the surface tension force exerted by the liquid bridge meniscus around the disk circumference, \tilde{F}_T . The capillary pressure represents the difference between the pressure within the liquid bridge and the pressure within the bath liquid. Thus, the total force, \tilde{F} , exerted by the bridge on the lower disk is given by

$$\tilde{F} = 2\pi R\gamma\sin\phi - \pi R^2\bar{\kappa}_0\gamma \quad (1)$$

where g is the gravitational acceleration, γ is the interfacial energy, ϕ is the contact angle, and $\bar{\kappa}_0$ is the mean curvature evaluated at $z=0$. Here the mean curvature is defined as

$$2\bar{\kappa} = -\nabla \cdot \mathbf{n}, \quad (2)$$

where \mathbf{n} is the outward pointing normal to the surface. (For an equivalent alternative definition see Appendix I.) For right circular cylindrical bridges, which can be formed only as $\Delta\rho \rightarrow 0$, the contact angle is $\pi/2$ and $\bar{\kappa} = 1/2R_0$. In this case the total force on the lower disk simplifies to

$$\tilde{F} = \pi R\gamma. \quad (3)$$

For a bridge in equilibrium, the mean curvature, $\bar{\kappa}$, must satisfy

$$p - p_0 - \Delta\rho g z = -2\bar{\kappa}\gamma, \quad (4)$$

where $\Delta\rho$ is the difference between the densities and pressures of the liquid bridge and the surrounding bath and $p - p_0$ is the difference between the pressure in the liquid bridge and the pressure in the bath at $z = 0$. This difference is equal to $-2\bar{\kappa}_0\gamma$.

We have solved equation (2) using an approach based on a method described by Myshkis et al. [9] and later by Slobozhanin and Perales [10]. The method is straightforward and details are given in Appendix I. In short, the surface is parameterized in terms of its arclength s . Three coupled nonlinear ordinary differential equations for the bridge radius, height and slope are generated by this parameterization. They are solved by a shooting method together with a Newton technique to satisfy a constant volume constraint. To calculate the curvature $\bar{\kappa}_0$ in equation (1) we must solve for the full equilibrium configuration of the bridge. We have carried out such calculations to compare with our experimental results. The computational procedure involves the solution of the bridge equilibrium shape for a given aspect ratio and volume. The values of the pressure difference $p - p_0$, and the contact angle, ϕ , at the lower disk are also obtained. These quantities are adjusted until the boundary conditions and constant volume constraint are satisfied (see Appendix I). The method has

been extended to perform stability calculations and is similar to the technique of Slobozhanin et al. [10].

In the following sections our experimental and computational results are described in terms of these dimensionless parameters: the dimensionless mean curvature $H_0 = \bar{\kappa}/R$, the aspect ratio $\Lambda = L/2R$, the relative volume, $V = (\text{actual volume})/\pi R^2 L$, and the dimensionless force $F = \tilde{F}/\pi R \gamma$.

3.2 Force measurement experiments

3.2.1 Materials

The silicone fluid, generously supplied by Dow Corning, is a bulk polymerized polydimethylsiloxane, with a dynamic viscosity of 100 cs. The fluid contains less than 0.5% volatile materials. The methanol-water solution consisted of methanol supplied by Fisher Chemical, and was certified to be acetone free, with less than 0.02% water content. Biological grade type I water was supplied from a Millipore RO[®] system coupled with a Milli-Q[®] deionizer.

3.2.2. Apparatus

A steel cantilever arm, length = 8.5 cm, diameter = 0.02286 cm, attached to a rigid support at one end and to a thin 1 cm diameter polycarbonate disk at the other allows the disk to move freely under an applied load. To track the disk motion, a piece of reflective plastic tubing located at 6.2 cm from the fixed end of the cantilever arm is used for diffuse reflection of a laser beam. The scattered light is collected by a 35 mm SR camera and an 80 mm macro zoom lens. A position sensitive photodiode is mounted at the film plane. We found, for this case, the maximum signal to noise ratio is obtained by a combination of maximum zoom and maximum defocus of the lens. The photodiode is connected to a United Detector Technology model 431 X-Y position monitor. Output from the monitor was sent to a chart recorder. The motion of the reflective plastic is proportional to that of the lower disk. The bridge motion is also recorded with a CCD video camera connected to a video monitor through a videocassette recorder. This allows direct measurement of the contact angle on the lower disk. Fluctuations in density of the bath are regularly monitored using a hydrometer. This is especially important when working at low Bond numbers.

To calculate the force from the measured deflection, it is assumed that the cantilever arm obeys Hooke's law. The modulus of elasticity of the cantilever arm was measured to be 30.42×10^6 psi, or 2.138×10^9 g/cm², and the effective spring constant was found to be 137.51 dyne/cm.

3.2.3 Procedure

Calibration

To calibrate how motion of the disk was related to motion of the chart pen, the lower and upper disks were connected by a thin film of silicone oil. Because the thin film pulls the

two disks together, the motion of the upper disk equals the motion of the lower disk, in the limit of small displacement. The upper disk was moved by computer controlled stepping motors moving along linear actuators. The precision of movement of the upper disk is 2.05×10^{-5} cm. The deflection of the chart pen was recorded and the position was held constant for two minutes to give a stable average reading. For small displacements (less than 0.25 cm) the motion of the pen was a linear function of the disk displacement (see Fig. 2). For larger displacements, a quadratic fit is necessary. This procedure was performed for each separate trial run.

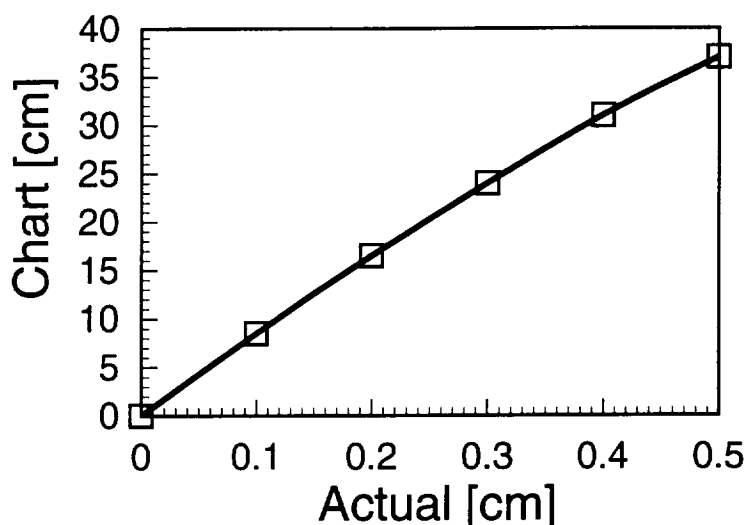


Fig. 2 Actual displacement versus Chart Displacement

Right Circular Cylindrical Bridges

Next we examined the forces exerted by right circular cylindrical bridges with different aspect ratios, and measured the displacement of the lower disk from its initial position. This was done by allowing the cantilever arm to establish its equilibrium position corresponding to the buoyancy force of the disk and wire relative to the bath. This position was recorded on the chart recorder. The upper feed disk was then brought into contact with the lower disk, and adjusted to bring the lower disk back to its equilibrium position. This eliminates any effect caused by the buoyancy of the cantilever arm. The density and temperature of the bath were measured and used to calculate the Bond number. Silicone oil was manually injected, and the upper feed disk moved until the bridge was a right circular cylinder. The aspect ratio was measured directly from the viewing monitor with calipers. The displacement of the lower disk was measured directly from the chart recorder. For right circular cylinders, the total force on the lower disk depends linearly on the product of the disk radius and the interfacial energy. This also allows us to measure the value of interfacial tension at very low Bond numbers,

which otherwise must be measured by more involved techniques such as the Wilhelmy plate method, or optical methods based on eigenfrequency excitations.

General Liquid Bridge Configurations

The final set of experiments involved mapping out sections of the Λ - V stability region for a given Bond number. Before creating each new bridge, the cantilever arm was brought to its equilibrium position. The computer controlled motors were used to inject specific amounts of oil and to displace the upper disk by a specified amount. The deflection of the lower disk was continuously recorded for a series of deformations. The physical parameters of the bridge (volume, aspect ratio) were calculated from records of motor and lower disk movement. From these measurements, the forces were calculated and checked against our theoretical predictions.

3.3 Results

Selected results are presented in Figs. 3-12. In each case, the force exerted on the lower disk by a constant volume bridge was examined for a range of aspect ratios. Two basic types of behavior are shown and depend on the relative volume V , the Bond number and the aspect ratio of the bridge. The Bond number affects both the contact angle at the lower disk and the capillary pressure. Together with each set of experimental results we have plotted the theoretical predictions for the force and the contact angle at the lower disk.

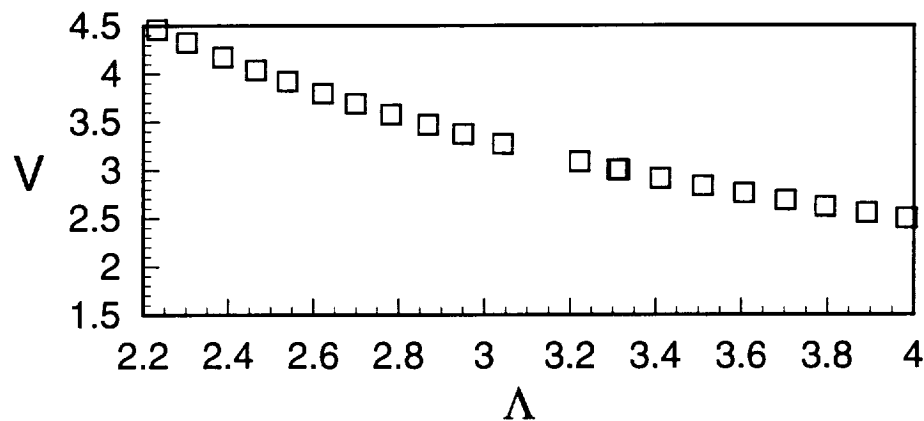


Fig. 3 Relative volume V versus aspect ratio, Λ , for Fig.4

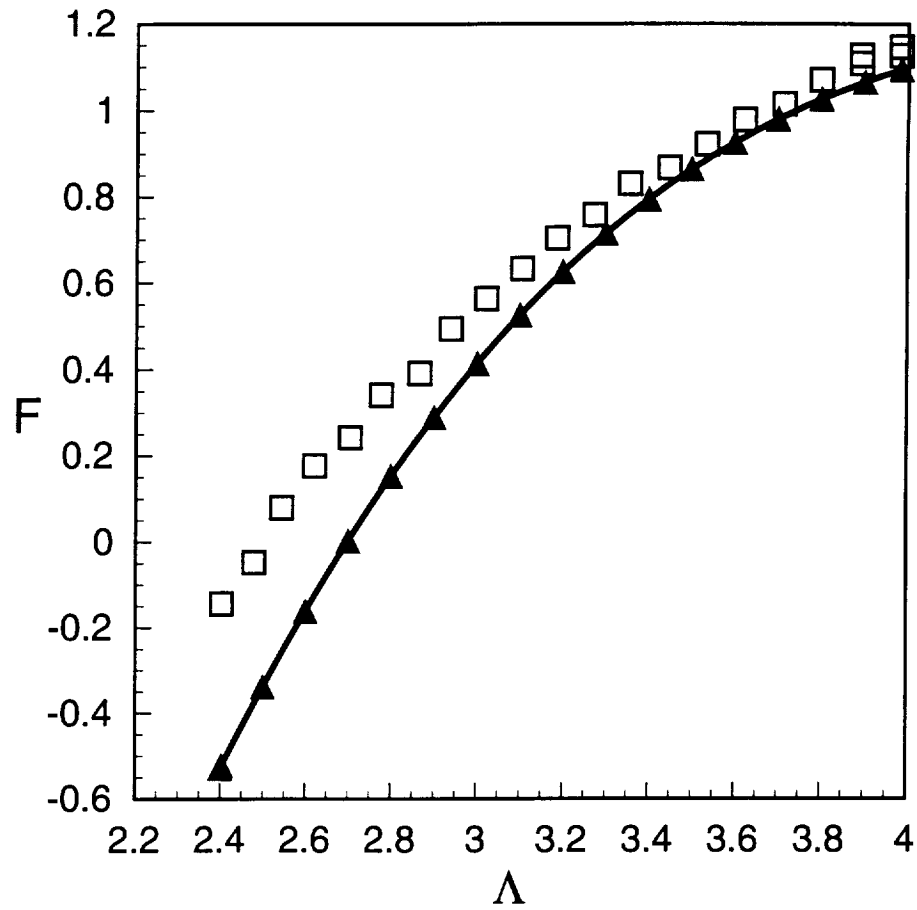


Fig. 4 Dimensionless force F versus aspect ratio Λ for a fixed volume bridge. The change of relative volume V with Λ is shown in Fig. 3. Experimental points are denoted by \square . Solid curve is fit to points (\blacktriangle) computed from theory.

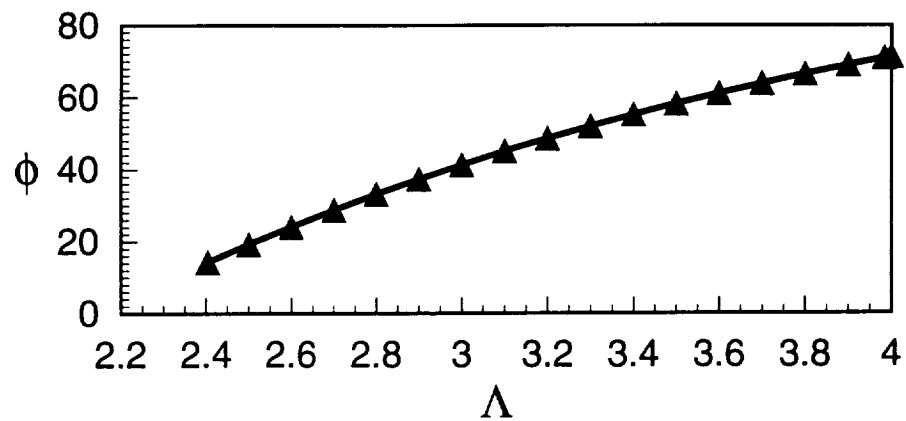


Fig. 5 Theoretical values of the contact angle ϕ as a function of aspect ratio Λ , computed for Fig. 4

Figures 3-5 show our results for a Bond number of 1.2×10^{-3} . The initial volume of the bridge is such that $V > 1$. As the aspect ratio is increased, the relative volume decreases to a final value of around 2.5 at aspect ratio 4. Initially, the small contact angle results in a weak upward tension. The large relative volume results in a stronger downward force and, thus, a negative force results. Note that the initial measured force appears to be about 20% of the theoretically predicted value. As Λ increases, the force increases. At an aspect ratio of approximately 2.5 the total measured force on the disk is almost zero. The calculated aspect ratio at which the force is zero is approximately 2.7. At this aspect ratio, the measured value of F is a little more than 0.2. Upon further extension, the measured values come closer to the theoretical ones. At the largest aspect ratio, the bridge is at the minimum volume stability limit for this Bond number and breakage occurs.

Figures 6-8 show similar results for $B = 0.015$. Once again there is a noticeable difference between the measured forces and the theoretically predicted ones as the force on the lower disk approaches zero. Notice that as the relative volume approaches unity, the dimensionless force F appears to be reaching a maximum. As in the previous case, the range of aspect ratios examined correspond to the maximum and minimum relative volume stability limits at this Bond number. It is worth noting that, in comparison to the first case, the theoretically calculated capillary pressure H_0 reaches a minimum value at $\Lambda = 2.7$. However, the force does not have a minimum since the contact angle is increasing at a rate which offsets the decrease in force due to the capillary pressure. Figure 12 shows the computed values of \tilde{F}_{CP} and \tilde{F}_T for each case.

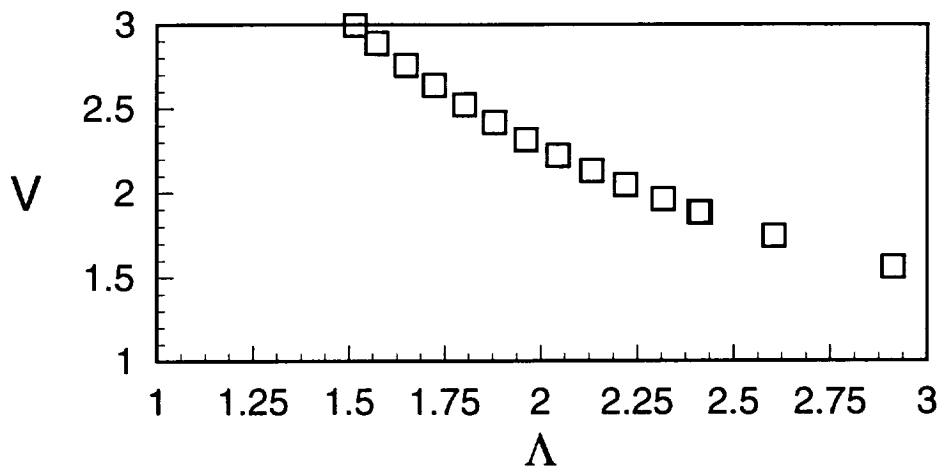


Fig. 6 Relative volume V versus aspect ratio, Λ , for Fig. 7

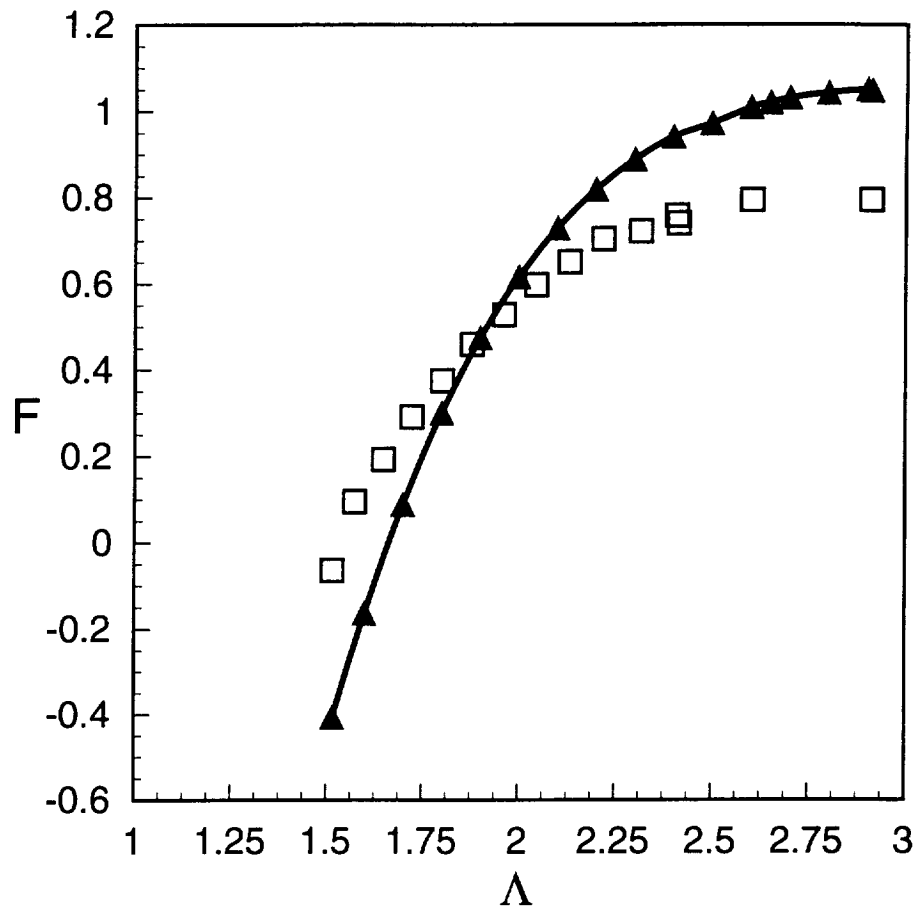


Fig. 7 Dimensionless force F versus aspect ratio Λ for a fixed volume bridge. The change of relative volume V with Λ is shown in Fig. 6. Experimental points are denoted by \square . Solid curve is fit to points (\blacktriangle) computed from theory.

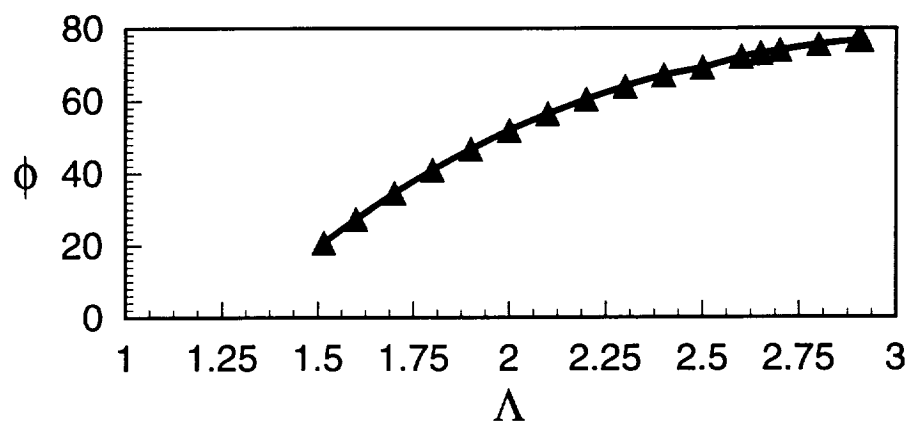


Fig. 8 Theoretical values of the contact angle ϕ as a function of aspect ratio Λ , computed for Fig. 7

Figures 9-11, show a lower volume bridge for which the relative volume decreases below unity and the contact angle exceeds 90° . Both experiment and theory are in agreement

as F approaches a maximum value at an aspect ratio in the neighborhood of 1.52. The contact angle reaches 89.93° at this point (see Fig. 11).

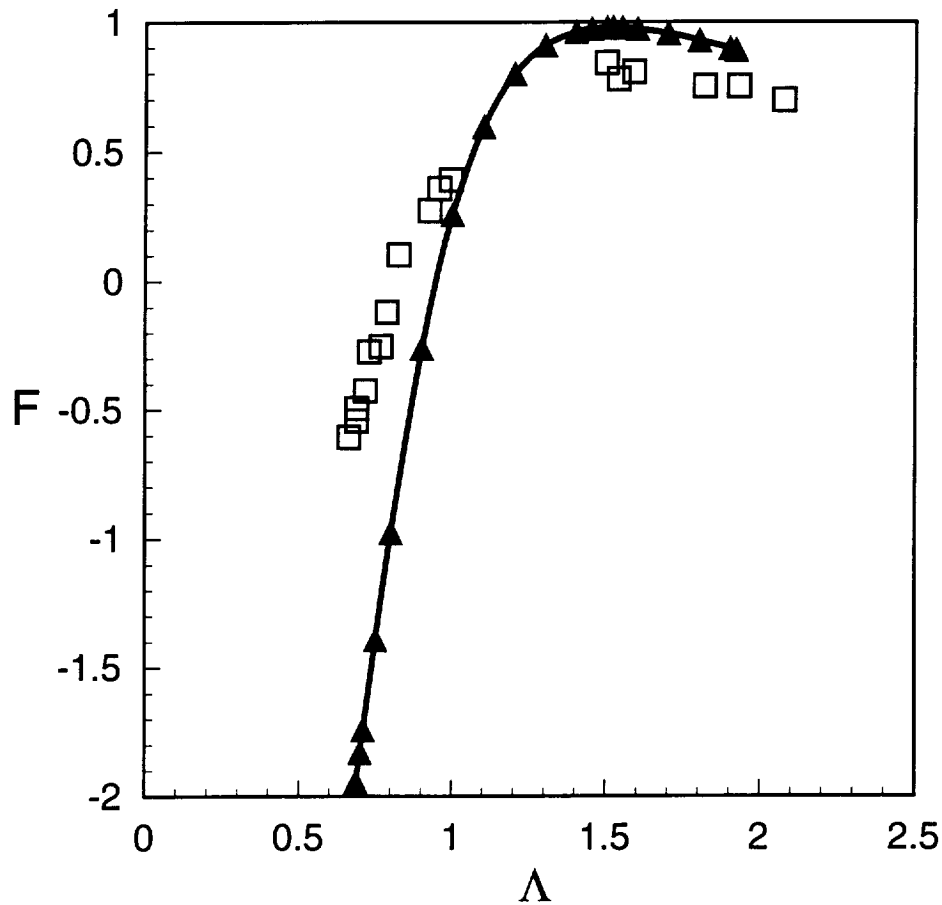


Fig. 9 Dimensionless force F versus aspect ratio Λ for a fixed volume bridge. The change of relative volume V with Λ is shown in Fig. 10, below. Experimental points are denoted by \square . Solid curve is fit to points (\blacktriangle) computed from theory.

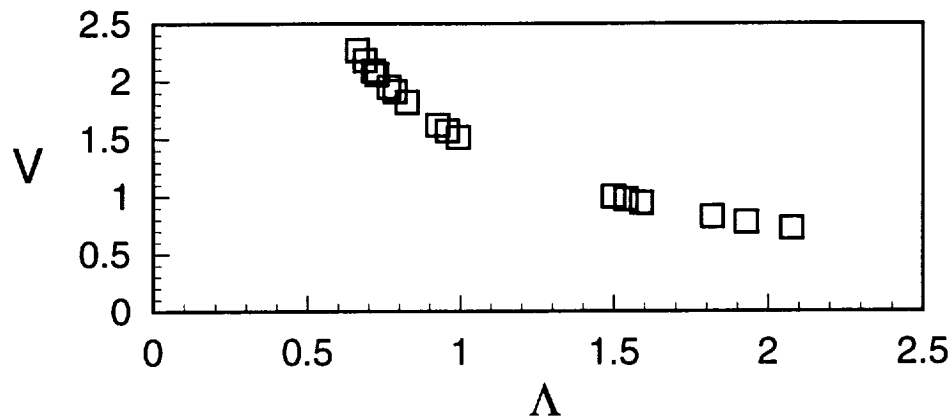


Fig. 11 Relative volume V versus aspect ratio, Λ , for Fig. 9

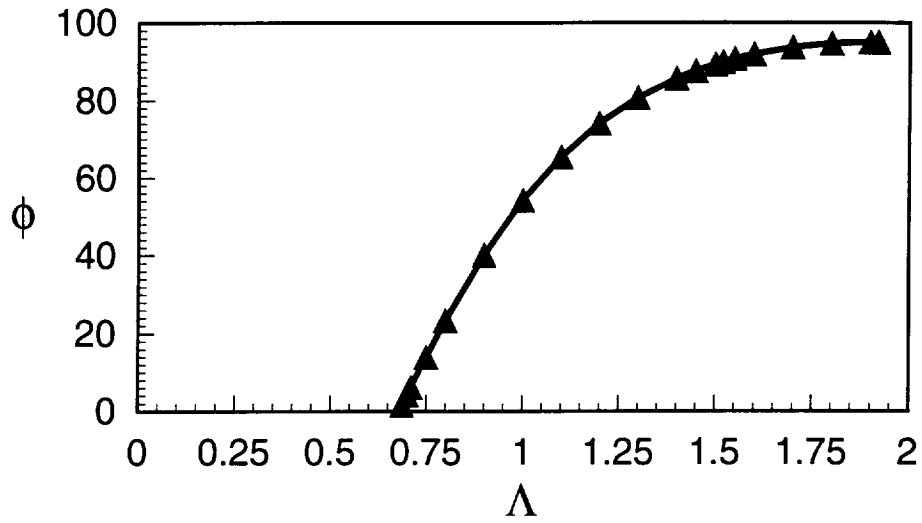


Fig. 11 Theoretical values of the contact angle ϕ as a function of aspect ratio Λ , computed for Fig. 9

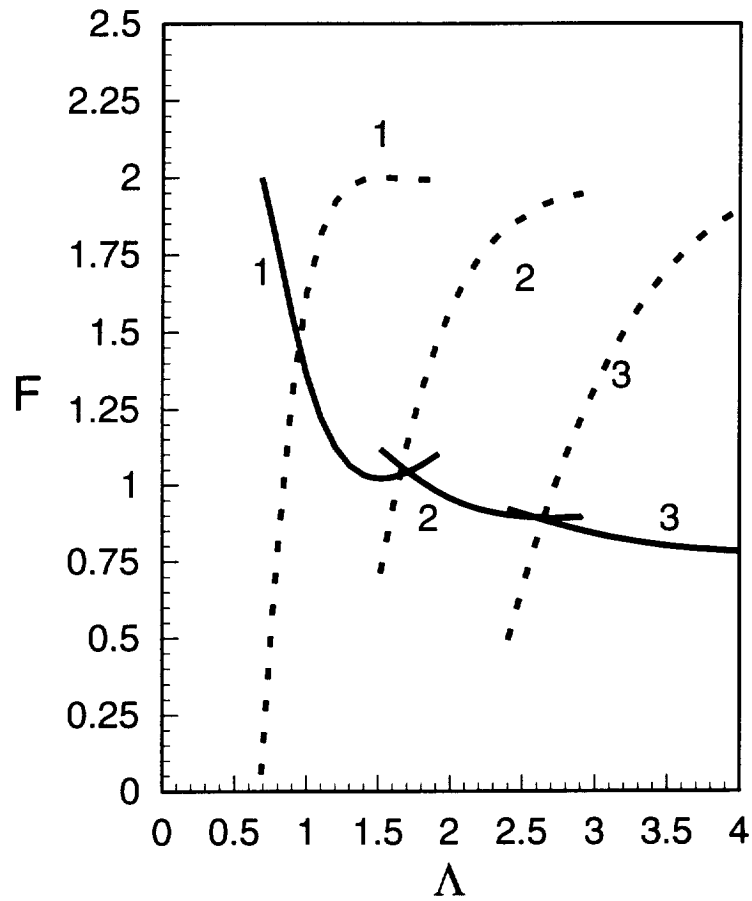


Fig. 12 Capillary pressure (solid lines) and meniscus tension (dashed lines) as a function of aspect ratio. The numbers correspond to the three cases shown earlier: 1- Fig. 10, 2- Fig. 6, 3- Fig. 3

Figure 12, shows the computed values of F_{CP} and F_T for the cases described. In two of the cases (1 and 2) F_{CP} reaches a minimum. The total force F , however does not exhibit a maximum for case 2, however, but does for case 1 that exhibits a maximum in F_T close to the minimum for F_{CP} at $\Lambda = 1.52$.

3.4 Discussion

We have measured the static and dynamic forces associated with a liquid bridge held between two coaxial equidimensional disks. The force acting upon the lower support disk was measured for various aspect ratios and volumes. Our measurements are in good agreement with theory except in the regions where the theoretical contact angles are small. It was shown that a minimum in capillary pressure does not always result in a maximum upward force on the lower disk, and that for a fixed actual volume, the bridge may not experience a minimum in capillary pressure as the aspect ratio is increased.

The resolution and noise level of the chart recorder give an error of ± 0.5 dyne on the total force. This may explain the discrepancy between the theoretical results and the experimental ones as the total force on the lower disk approaches zero. An additional but much smaller error is caused by misalignment of the lower disk. The maximum misalignment is 5 degrees. This corresponds to an error in the measured force of approximately 0.8%. The uncertainty of the Bond number translates into an error in the buoyancy force of $g\Delta Bo = 7 \times 10^{-2}$ dyne. The errors due to uncertainties in physical parameters of the bridge itself (volume, aspect ratio) place an additional 1% error in the measurements.

These error sources are small in comparison with the wetting problem at the sharp disk edges. As mentioned earlier, at a perfectly sharp edge, the contact line is pinned, but the contact angle can take on a range of values. For rough edges this may not be the case, and the contact line may prematurely slip over the disk edge. This has two effects. First, the volume of the bridge is reduced. This will lead to a reduction in the capillary pressure. Furthermore, the upward force on the lower disk due to the surface tension will not decrease as readily. This is because the contact angle will not decrease with decreasing aspect ratio as rapidly as theory predicts. We will replace the polycarbonate disk with a carefully machined steel disk, similar to that used for the upper bridge support.

4. THEORY AND SIMULATION

Our theoretical and numerical simulation work has been progressing well. Four lines of research were in progress during the second year:

- 1) Dynamic stability of long liquid bridges
- 2) Stability of liquid bridges to nonaxial gravity

3) Nonaxisymmetric bridge dynamics: code development

Work in the first area has been described in past reports and is the subject of a recently published paper (See Appendix). Progress in the other three areas along with selected results is described below.

4.1 Effect of nonaxial acceleration on liquid bridge stability

Chen and Saghir [11] examined the effect of a lateral Bond number on small liquid bridges held between coaxial equidimensional disks. We extended their analysis as part of our code development for 3D bridge dynamics. Our results were described briefly at the Fluid Physics meeting at NASA-LeRC earlier this year and are summarized in Figs. 13-15. Here, the stability limits were found by changing the bridge volume at fixed aspect ratio until the bridge “broke”. For the computational method under consideration this generally meant that the solutions failed to converge, or that negative radii were computed. These results, which are for slender bridges show that the minimum volume stability limit is substantially modified as the lateral component of acceleration is increased and appears to approach, but not meet, the “zero Bond number” minimum volume limit.

The criterion used to determine stability for these cases is really not satisfactory since lack of convergence may not reflect physical behavior. We have since extended this analysis using the code *Surface Evolver* [12]. This method is better suited to the problem of bridge equilibrium configurations in that it is faster than our 3D code. Thus, we are using *Evolver* to continue our study of the problem of nonaxial bridge stability. After verifying our results shown in Figs. 13-15, we considered the problem of purely lateral acceleration. Results for $B=0.1$ are shown in Fig. 14, and typical bridge profiles are shown in subsequent figures.

The minimum volume limit is substantially modified at higher values of Λ . At lower Λ , the minimum volume limit is indistinguishable from the zero-g limit for axisymmetric bridges. The maximum volume limit is modified extensively. Indeed, in contrast to axisymmetric bridges, the volume stability limit $V \rightarrow \infty$ as the aspect ratio $\Lambda \rightarrow 0$, rather than $V \rightarrow 1$. This is because a large relative volume of liquid can essentially “hang” from the two circular disks. As the separation distance approaches 0 this volume remains finite and the relative volume $V \rightarrow \infty$ (see Fig. 16). An alternative representation of the stability diagram is shown in Fig. 17 where the volume $V^* = 2\Lambda V$ remains constant as Λ is changed.

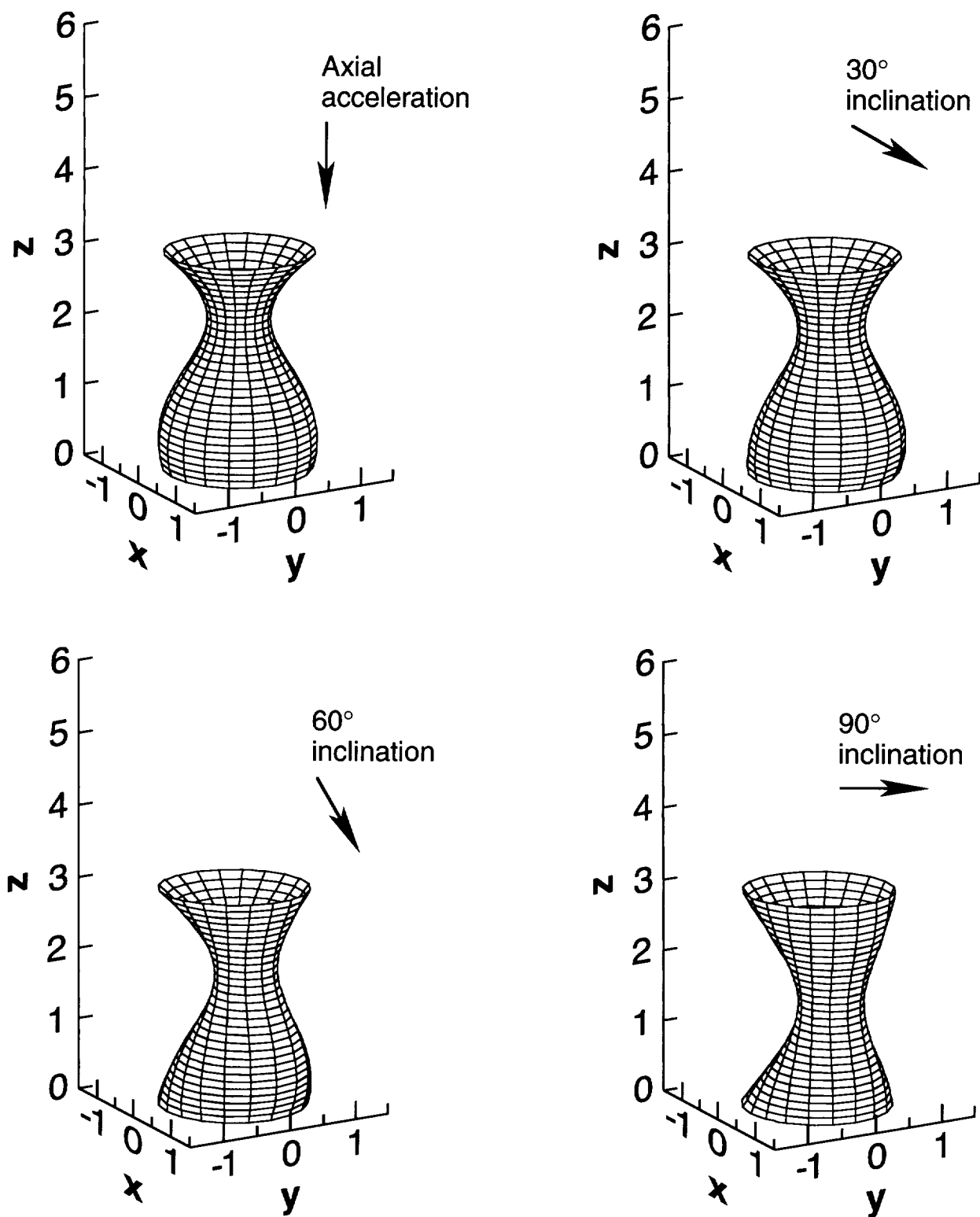


Figure 13. Liquid bridge shapes for different inclinations of the gravity vector $Bo = 0.5$, $\Lambda = 1.5$.

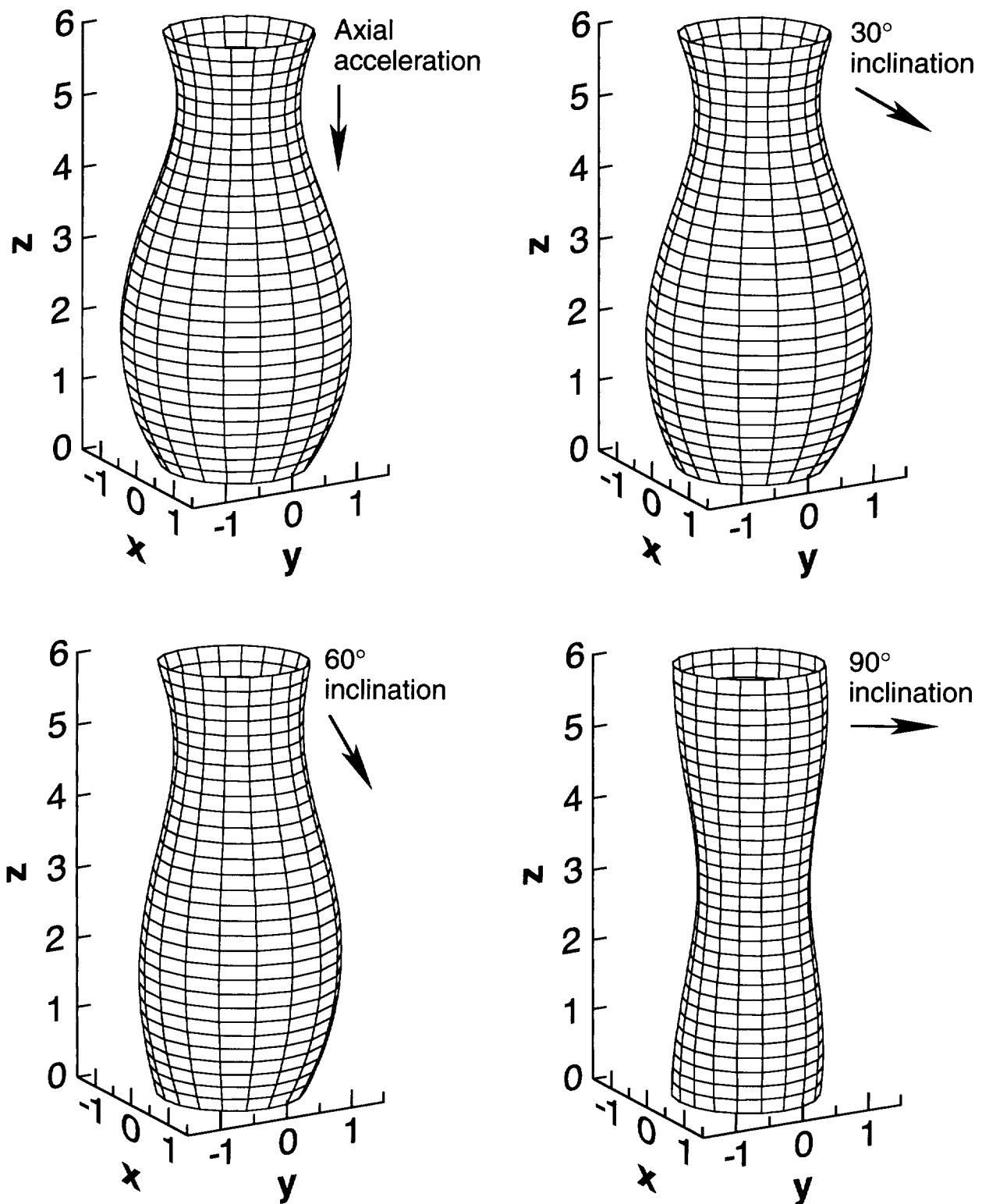


Figure 14. Liquid bridge shapes for different inclinations of the gravity vector $Bo = 0.05$, $\Lambda = 3$.

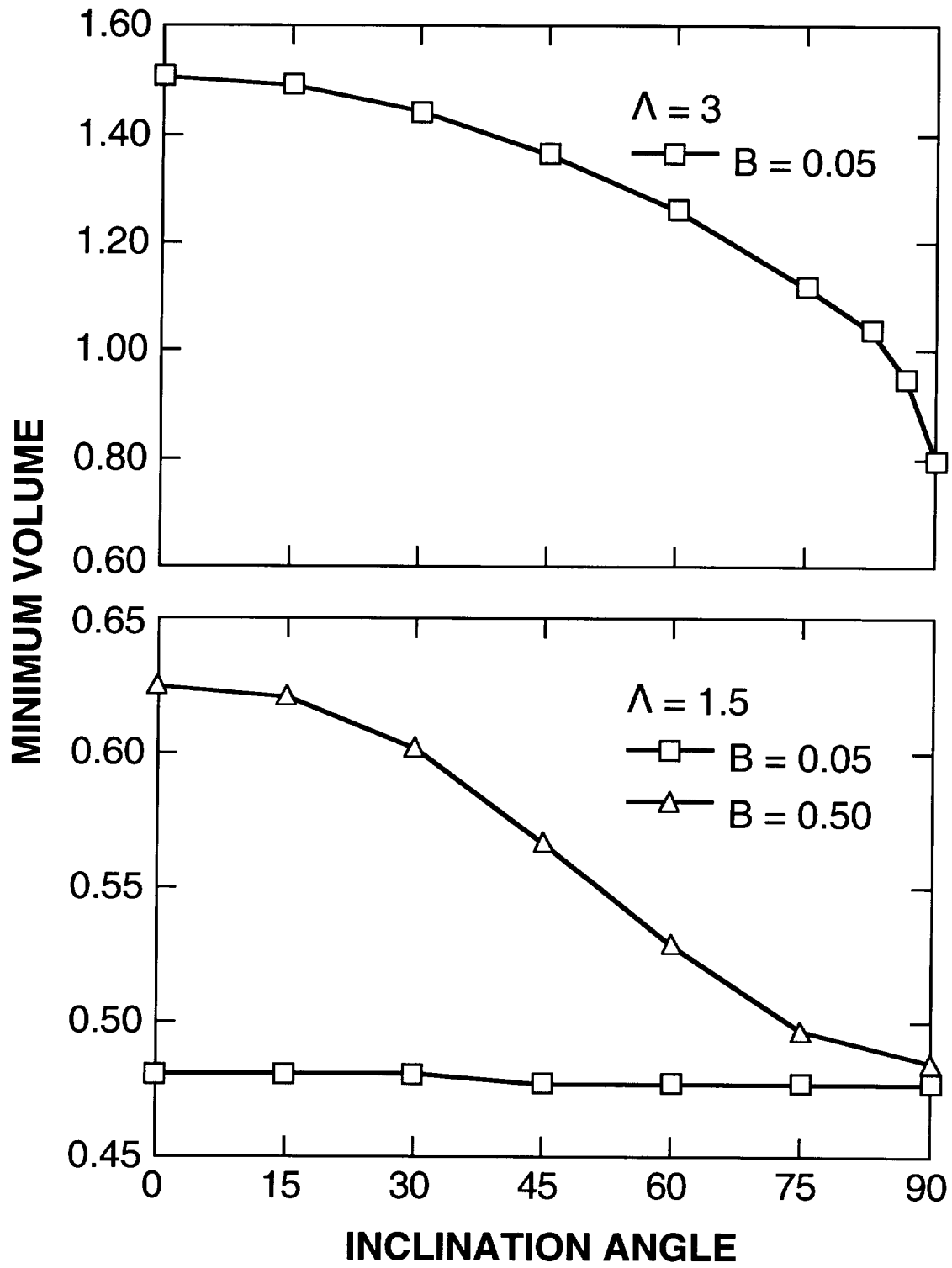


Figure 15. Effect of inclination angle on the minimum stable volume at fixed Bo and aspect ratio.

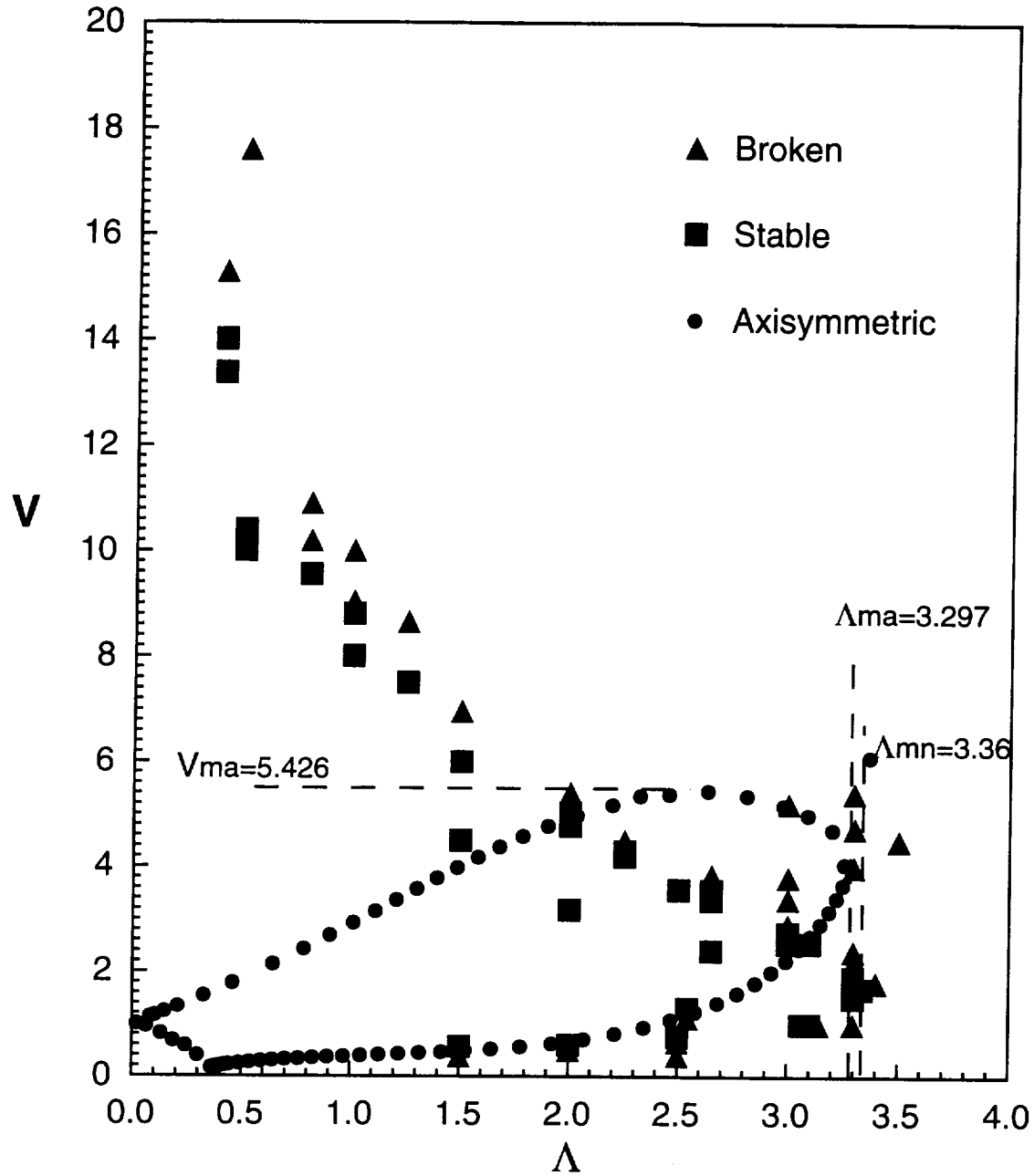


Fig. 16 Stable and unstable bridges for lateral gravity as a function of relative volume V and aspect ratio Λ for $Bo=0.1$. The locus of the points shown as circles describes the stability margin for axial acceleration at $Bo=0.1$, Λ_{ma} and V_{ma} are the maximum values of V and Λ for the axisymmetric cases with $Bo=0.1$, Λ_{mn} is the maximum Λ for the lateral acceleration

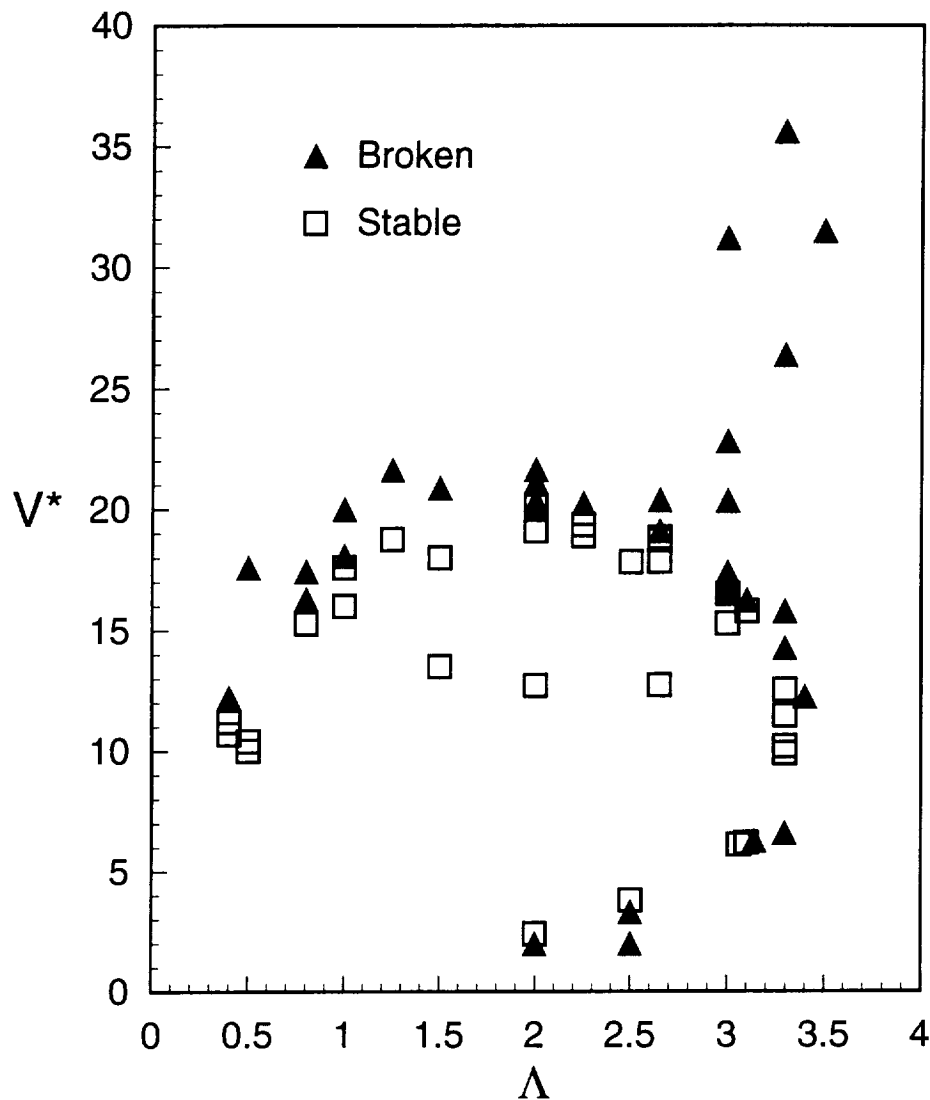


Fig. 17 V^* versus Λ an alternative representation of the stability region for lateral gravity shown in Fig. 17 for $Bo=0.1$

Selected examples of the bridge shapes are shown in Figs. 18-23. Figures 18 and 19 show slender bridges with $V < 1$. Both examples were found to be unstable and broke by “pinching” off in the middle, leaving two separate drops, each attached to the support disks. This is consistent with the typical axisymmetric breaking observed with such bridges under axial gravity at the minimum volume stability limit where axisymmetric perturbations are the most dangerous [10]. Figure 20 shows four different views of the same bridge at large V and aspect ratio 1. The bridge is close to the stability limit but stable. The bridge shows a typically bulbous shape with the bulk of the liquid hanging outside the two support disks. Note the two “dimples” that are present where the top of the hanging volume meets the supporting disks. The bridge takes on the appearance of a pendant drop and the liquid

furthest from the disks tends to take on a quasi-spherical form. Figure 21 shows two unstable pendant bridges. The sequence of shapes computed along the trajectory to the minimum energy configuration leads to the larger volume pinching off and leaving a smaller volume attached to the each disk. Figure 22 shows a stable pendant bridge with a relative volume of 13.69 and an aspect ratio of 0.4. This illustrates how, even as the aspect ratio decreases, the volume of liquid that can be held between the disks is still large. Thus as the separation distance L between the disks decreases (forcing $\Lambda \rightarrow 0$) the relative volume V tends to infinity (note that V^* is constant, see Fig. 17). Figure 23 shows a stable long aspect ratio bridge that is close to the stability margin. It represents the maximum value of Λ we were able to compute for $Bo=0.1$ under lateral gravity conditions.

Work on the stability of bridges subjected to nonaxial gravity will continue during the third year. We expect this to be a fruitful area of investigation. Our ongoing work includes an investigation of the effect of Bond number magnitude and on the importance ratio between the lateral Bond number and the axial Bond number.

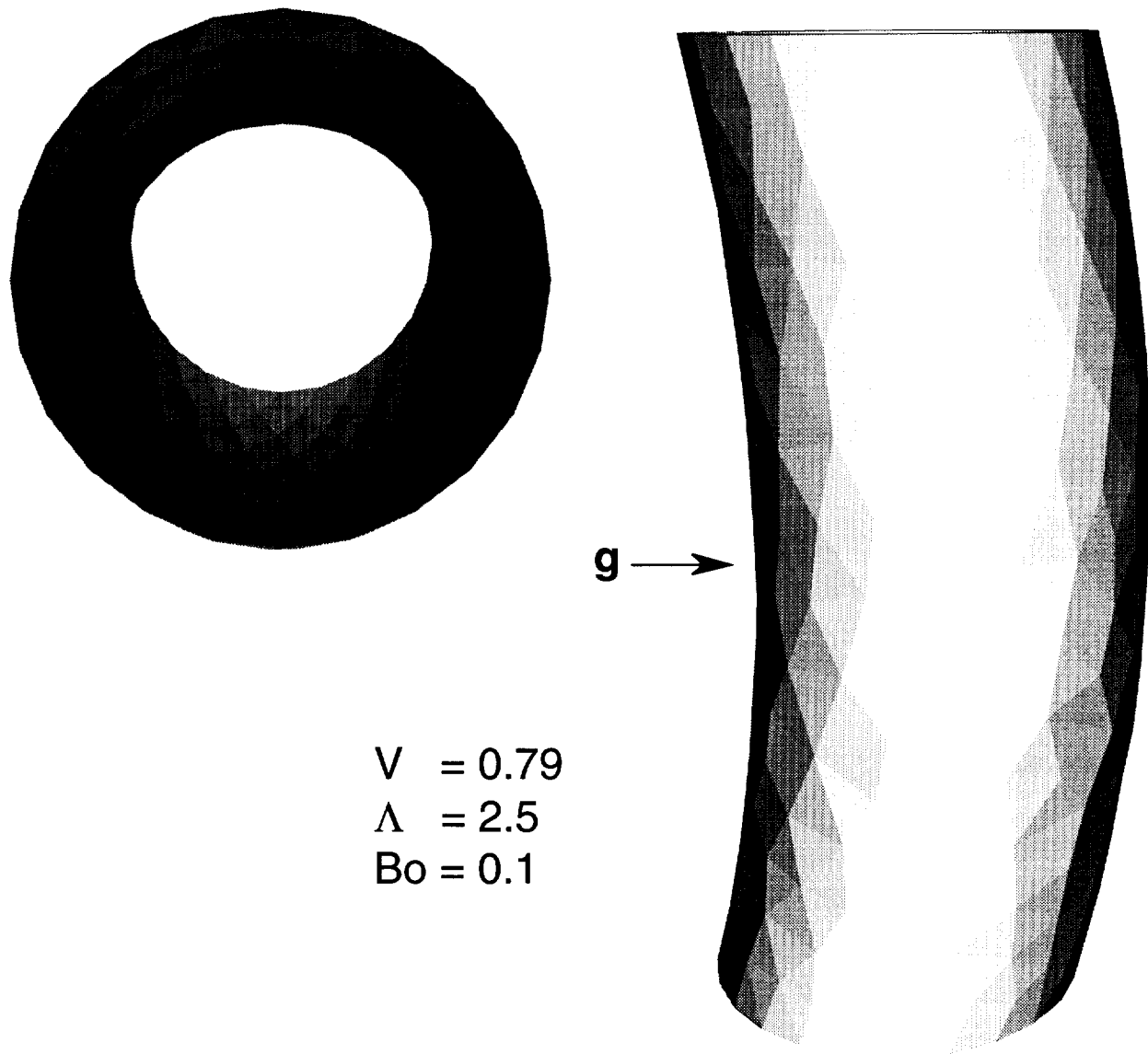


Figure 18. An unstable slender low volume bridge. The bridge evolves to two separate drops attached to the support disks.

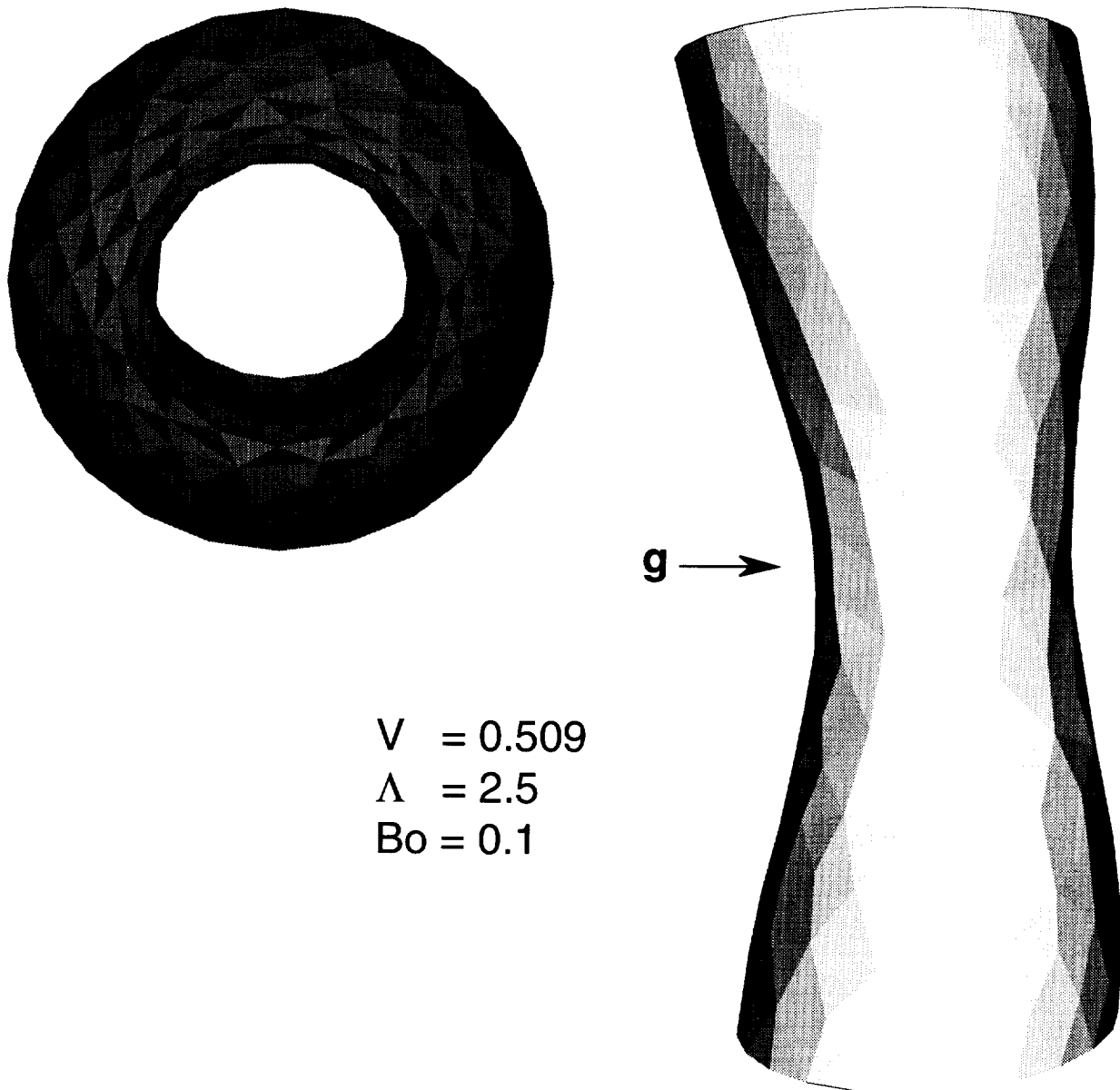


Figure 19. An unstable slender low volume bridge. The bridge evolves rapidly to two separate drops attached to the support disks.

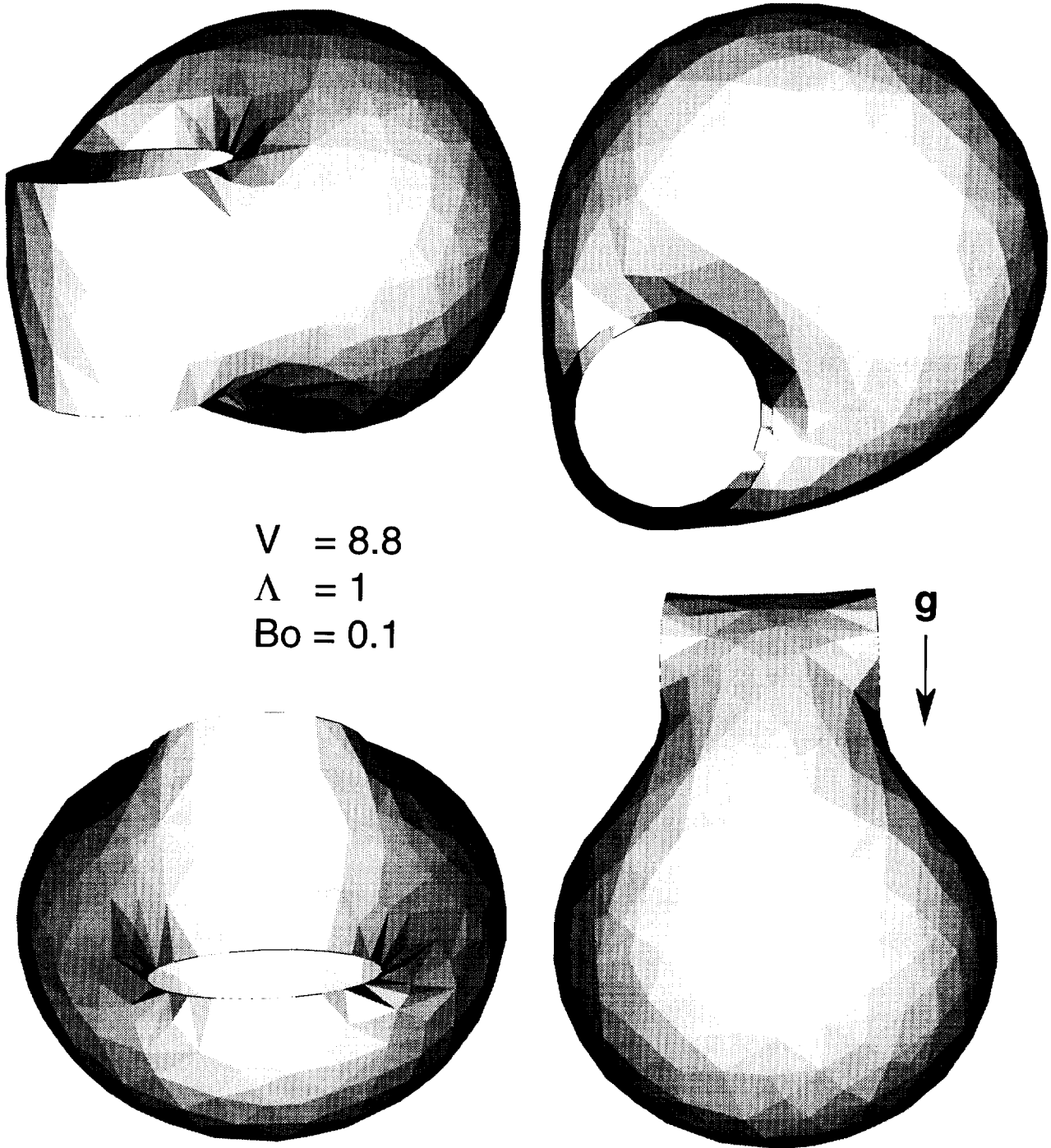


Figure 20. Four different views of the same stable birdge at large V .

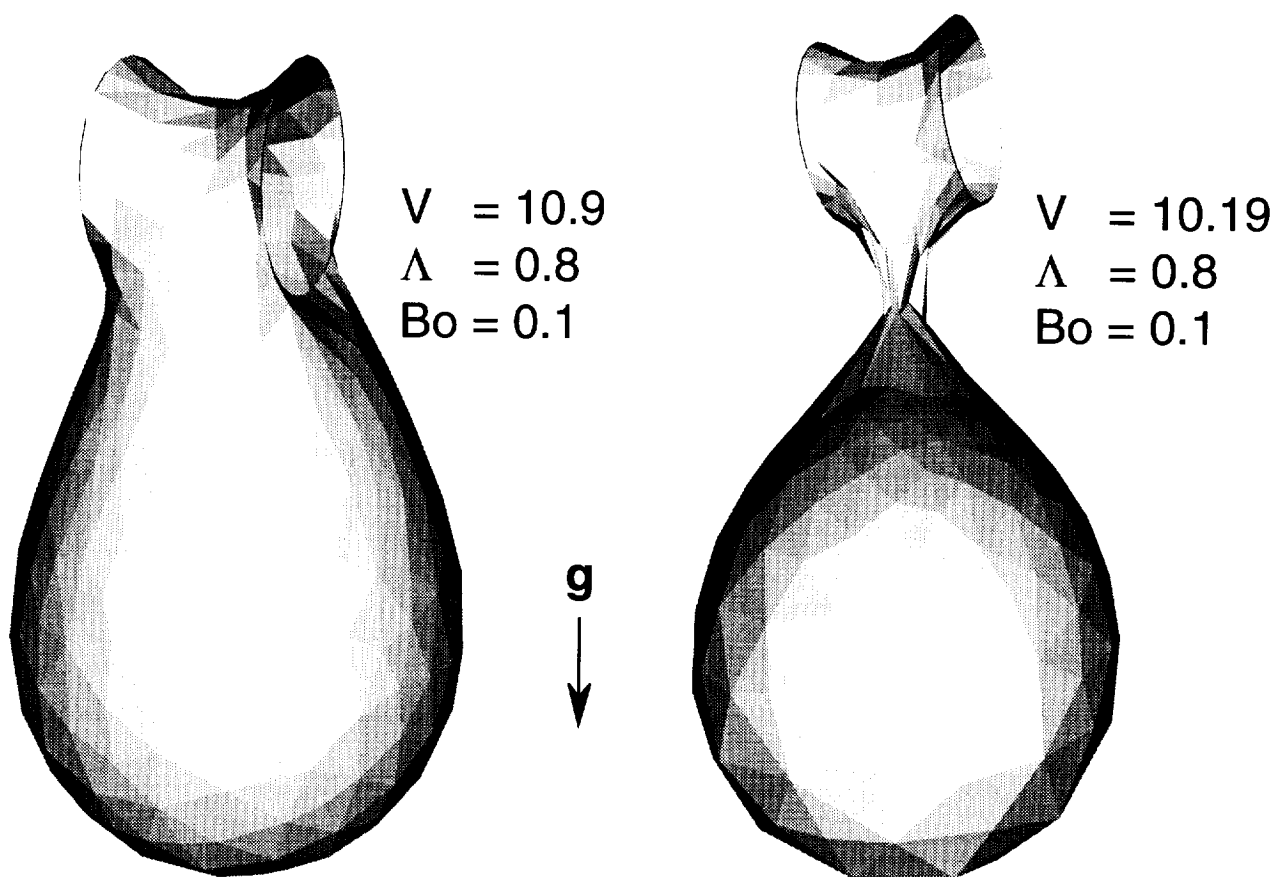


Figure 21. Two unstable pendant bridges.

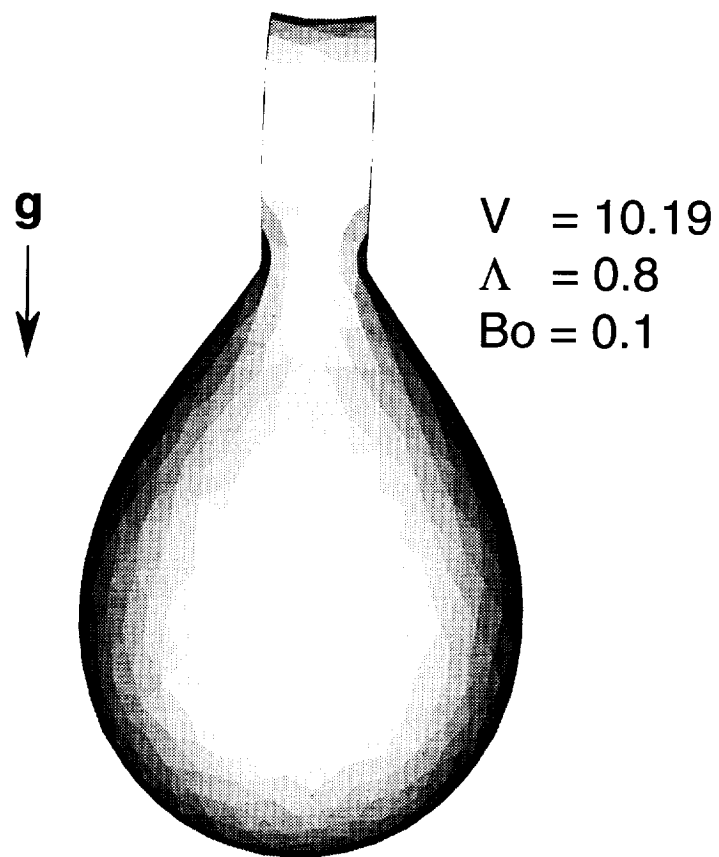


Figure 22. A stable pendant bridge.

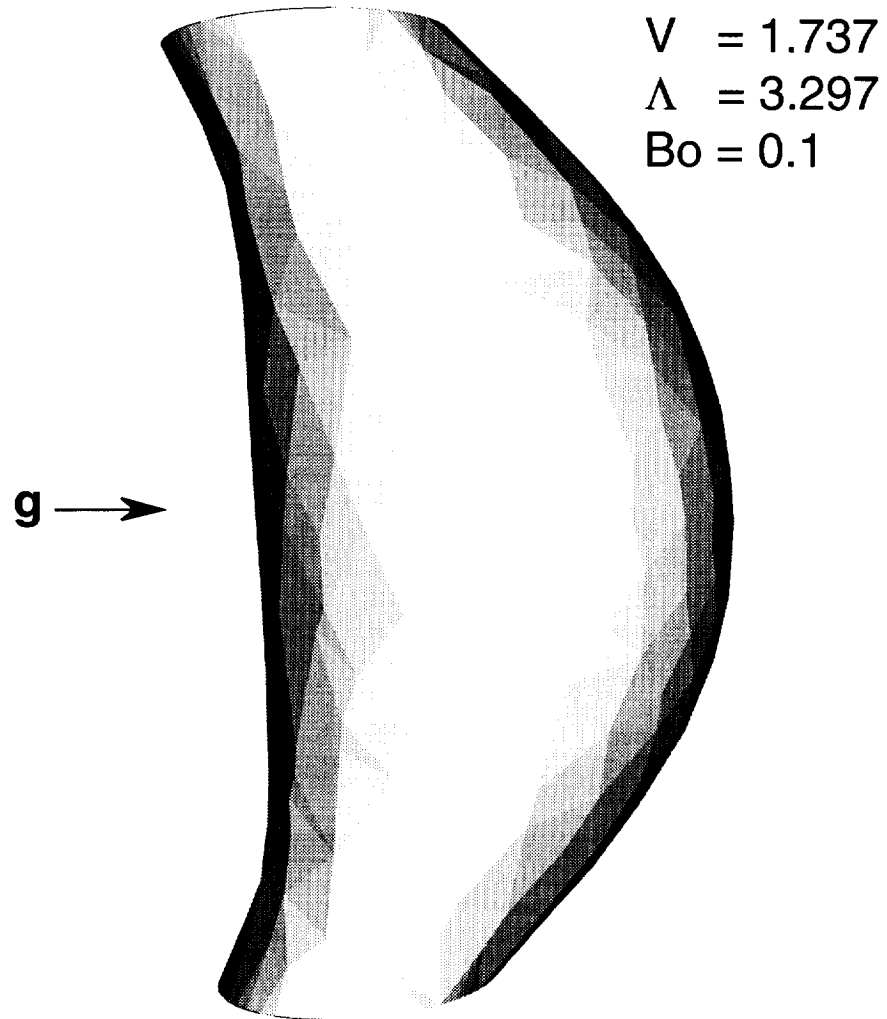


Figure 23. A stable bridge with the maximum slenderness computed for $Bo = 0.1$.

4.4 Three dimensional dynamical simulations

Our work in this area is motivated by our study of experimental axisymmetric and non-axisymmetric oscillations of liquid bridges. The problem is to solve the equations governing the conservation of linear momentum in a homogeneous isothermal Newtonian viscous liquid bridge. The location of the free surface of the bridge is time-dependent on time must be found as part of the solution to the problem. In earlier work we undertook numerical simulation of 2D axisymmetric models of liquid bridge vibration using a method based on finite differences. A Picard iterative approach was used to deal with the free surface. In parallel, we have developed a code capable of 3D simulation of bridge vibration. It is based on a “volume of fluid method” (VOF) [14]. The VOF method is combined with the continuum surface force (CSF) model of Brackbill et al. [15] to account for surface tension effects. The CSF model represents the interface between two fluids as a transition region of finite thickness across which the fluid properties vary continuously. The surface tension is treated as a continuous 3D effects across this transition region and in this sense is modelled as a volume force.

The basic equations are spatially discretized using the implicit finite volume approach [13]. Here the viscous and convection terms are approximated using second order accurate central differences and upwind differences, respectively. A distribution function that defines the interface within a control volume is used to track the location of the surface of the liquid bridge. For the solution of this function a third-order upwind scheme [17] is used.

An iterative scheme is used to advance the integration of the discretized governing equations and boundary conditions in time. At each time step, the system of algebraic equations resulting from the spatial and temporal discretization is solved using a preconditioned general conjugate residual method or a conjugate gradient squared method. Both these techniques have been adapted to cope with the cyclic boundary condition arising from the azimuthal shape of the liquid bridge.

The method has been used to calculate 3D oscillations of a liquid bridge subject to a nonaxial vibration of the supporting disks. We are currently working on improving the code in terms of performance and accuracy and we are modifying it in an attempt to calculate the bridge breaking process. The code and our results will be described in more detail in the next semi-annual report.

5. PUBLICATIONS AND CONFERENCE PRESENTATIONS

Papers published and in preparation

- J. Meseguer, M.A. Gonzalez and J.I.D. Alexander, *Dynamic stability of long axisymmetric bridges*, **Microgravity Science and Technology**, VII, 234-242, 1994.
- J.I.D. Alexander, A. Resnick, W.F. Kaukler and A. Fedoseyev, *Force measurements on liquid bridges*, to be submitted to **Journal of Colloid and Interface Science**, 1994.
- J.I.D. Alexander, A. Resnick, W. F. Kaukler and Y.Q. Zhang, *Dynamics and Statics of Nonaxisymmetric and Symmetric Liquid Bridges*, Proceedings of the Second Microgravity Fluid Physics Conference, Cleveland, June 21-23, 1994.
- J.I.D. Alexander and Y.Q. Zhang, *Stability of liquid bridges subject to nonaxial gravity*, manuscript in preparation, 1994
- J.I.D. Alexander and Y.Q. Zhang, *A VOF-CSF method for 3D liquid bridge dynamics*, manuscript in preparation, 1994

Presentations at conferences and workshops

- J.I.D. Alexander, *Stability of nonaxisymmetric liquid bridges*, Invited presentation at the European Low Gravity Research Association Biannual Meeting (ELGRA), Madrid, Spain, December 11-14, 1994.
- J.I.D. Alexander, *Dynamics and Statics of Nonaxisymmetric and Symmetric Liquid Bridges*, Proceedings of the Second Microgravity Fluid Physics Conference, Cleveland, June 21-23, 1994.

6. WORK PLANNED FOR THE THIRD YEAR

We plan to continue the theoretical and experimental work described in the previous sections. In particular, we expect to be able to report in more detail on our experimental work on vibration and on our theoretical efforts concerning bridge dynamics, and on nonaxisymmetric stability.

7. REFERENCES

- [1] D.N. Mazzone, G. I. Tardos and R. Pfeffer, *Powder Technology* **51** (1987) 71.
- [2] H. Schubert, in *Agglomeration* 77, K.V. Sastry ed. (AIME, 1977) 144.
- [3] K. Hotta, K. Takeda and K. Inoya, *Powder Technology* **10** (1974) 231.
- [4] W.B. Putsch, E. Hoffman and H. Rumph, *I&EC Prod. Res. Devel.* **8** (1969) 58.
- [5] L.A. Adorjan, in *Agglomeration* 77, K.V. Sastry ed. (AIME, 1977) 130.
- [6] F.R. De Bisschop and W.J.L. Rigole, *J. Colloid Interface Sci.* **88** (1982) 117.
- [7] D.N. Mazzone, G. I. Tardos and R. Pfeffer, *J. Colloid Interface Sci.* **113** (1986) 544.
- [8] E. Wolfram and J. Pinter, *Acta Chim. Acad. Sci. Hung.* **100** (1979) 28.
- [9] A.D. Myshkis, V.G. Babskii, N.D. Kopachevskii, L. A. Slobozhanin and A.D. Typustov, *Low Gravity Fluid Mechanics* (Springer Verlag, Berlin, 1976) 583 pp.
- [10] L. A. Slobozhanin and J.-M. Perales, *Phys. Fluids A*, **5** (1993) 1305.
- [11] H. Chen and M.Z. Saghir, *Microgr. Sci. Technol.*, **7** (1994) 12.
- [12] K. Brakke, *Experimental Mathematics* **1**(1992) 141.

- [13] S.V. Patankar, *Numerical Heat Transfer and Fluid Flow* (Hemisphere, New York, 1980).
- [14] C. W. Hirt and B.R. Nichols, J. Comp. Physics **39** (1981) 201.
- [15] J. U. Brackbill, D.B. Kothe and C. Zemach, J. Comp. Physics **100** (1992) 335.
- [16] S.R. Chakravarthy, *AIAA Proceedings 23rd Aerospace Sciences Meeting*, January 10-14, 1985, Reno.

Appendix I

CALCULATION OF THE FORCES EXERTED BY AN AXISYMMETRIC LIQUID BRIDGE ON ITS SUPPORTS

1.1 Introduction

Consider an axisymmetric liquid bridge held between coaxial equidimensional disks of radius R . A cylindrical coordinate system (r, θ, z) is chosen such that the axis of the bridge lies parallel to the z -coordinate and $(0,0,0)$ lies at the center of the lower supporting disk. The bridge is acted on by a gravity vector oriented anti-parallel to the positive z -axis. For the bridge configuration shown in Fig. 1 of section 3, the forces acting on the lower disk consist of the capillary pressure and the component of force due to surface tension acting around the circumference of the disk acting in the z -direction. The capillary pressure is simply the pressure difference between the bridge liquid and the surrounding bath liquid. For non-zero Bond numbers, the capillary pressure will vary with height above the lower disk and is equal to the product of the surface tension and the mean curvature at that height. The resultant of these two forces is balanced by the force exerted by the deflected cantilever arm. In the experimental work described in section 3, the forces are measured for different bridge configurations. To calculate these forces, we need to know the capillary pressure and the contact angle associated with the Bond number, aspect ratio Λ and relative volume, V . The capillary pressure and the contact angle are determined by finding the equilibrium shape of the bridge for that (Λ, V) . To show how we obtain the governing equations, we first consider the following geometric quantities associated with the surface.

1.2 Fundamental magnitudes an mean curvature

First order magnitudes

Let u and v be parameters that describe the surface which is the locus of a point $\mathbf{r} = \mathbf{r}(u, v)$. Here $(u, v) \in \mathcal{R}$, where \mathcal{R} is the set of real numbers. For our axisymmetric liquid bridge surface we will introduce a cylindrical coordinate system (r, θ, ζ) and let z coincide with the symmetry axis. The axisymmetric equilibrium shape is defined by a line Γ that is the intersection between the surface and the half-plane $\theta = \text{constant}$. Now we define

$$\mathbf{r}_1 = \frac{\partial \mathbf{r}}{\partial u}, \mathbf{r}_2 = \frac{\partial \mathbf{r}}{\partial v}, \mathbf{r}_{11} = \frac{\partial^2 \mathbf{r}}{\partial u^2}, \mathbf{r}_{22} = \frac{\partial^2 \mathbf{r}}{\partial v^2}, \mathbf{r}_{12} = \frac{\partial^2 \mathbf{r}}{\partial u \partial v}, \quad (\text{I.1})$$

$$d\mathbf{r} = \mathbf{r}_1 du + \mathbf{r}_2 dv \quad (\text{I.2})$$

$$ds^2 = d\mathbf{r} \cdot d\mathbf{r} = |\mathbf{r}_1|^2 du^2 + |\mathbf{r}_2|^2 dv^2 + 2\mathbf{r}_1 \cdot \mathbf{r}_2 du dv = E du^2 + 2F du dv + G dv^2. \quad (\text{I.3})$$

Here E, F and G are the *fundamental magnitudes of first order*. They are related through

$$H^2 = EG - F^2 > 0, \forall (u, v) \in \mathcal{R}. \quad (\text{I.4})$$

Now the curves u and v cut an angle ω given by

$$\cos \omega = \frac{\mathbf{r}_1 \cdot \mathbf{r}_2}{\sqrt{EG}} = \frac{F}{\sqrt{EG}}. \quad (\text{I.5})$$

It follows that

$$\sin \omega = \frac{\sqrt{EG - F^2}}{\sqrt{EG}} = \frac{H}{\sqrt{EG}}. \quad (\text{I.6})$$

and

$$\sin \omega = \frac{|\mathbf{r}_1 \wedge \mathbf{r}_2|}{\sqrt{EG}} \Rightarrow H = |\mathbf{r}_1 \wedge \mathbf{r}_2|. \quad (\text{I.7})$$

The unit normal vector to the surface is given by

$$\mathbf{n}(u,v) = \frac{\mathbf{r}_1 \wedge \mathbf{r}_2}{H}. \quad (\text{I.8})$$

When u and v are orthogonal, $F=0$ and $H = \sqrt{EG}$.

Second order magnitudes

To obtain these quantities we use the fact that $\mathbf{n} \cdot \mathbf{r}_1 = \mathbf{n} \cdot \mathbf{r}_2 = 0$. Upon differentiation of the latter we have

$$\mathbf{r}_1 \cdot \mathbf{n}_1 = -\mathbf{n} \cdot \mathbf{r}_{11}, \mathbf{r}_1 \cdot \mathbf{n}_2 = -\mathbf{n} \cdot \mathbf{r}_{12}, \mathbf{r}_2 \cdot \mathbf{n}_2 = -\mathbf{n} \cdot \mathbf{r}_{22}, \dots \quad (\text{I.9})$$

The fundamental magnitudes of second order are the resolved parts of the vectors \mathbf{r}_{11} , \mathbf{r}_{22} , \mathbf{r}_{12} in the direction normal to the surface; That is,

$$\begin{aligned} L &= \mathbf{n} \cdot \mathbf{r}_{11}, M = \mathbf{n} \cdot \mathbf{r}_{12}, \mathbf{r}_2 \cdot \mathbf{n}_2 = N = \mathbf{n} \cdot \mathbf{r}_{22}, \\ \mathbf{r}_1 \cdot \mathbf{n}_1 &= -L, \mathbf{r}_1 \cdot \mathbf{n}_2 = -M, \mathbf{r}_2 \cdot \mathbf{n}_2 = -N. \end{aligned} \quad (\text{I.10})$$

Principal curvatures and mean curvature

For an curve C in the surface we can define a curvature vector \mathbf{k} [I.1] as

$$\frac{d\mathbf{t}}{ds} = \mathbf{k}, \quad (\text{I.11})$$

where $\mathbf{t} = d\mathbf{r}/ds$. The component of \mathbf{k} normal to the surface is called the normal curvature vector, its magnitude is defined as

$$\kappa_n = \frac{d\mathbf{t}}{ds} \cdot \mathbf{n} = -\mathbf{t} \cdot \frac{d\mathbf{n}}{ds} = -\frac{d\mathbf{r}}{ds} \cdot \frac{d\mathbf{n}}{ds} = -\frac{d\mathbf{r} \cdot d\mathbf{n}}{d\mathbf{r} \cdot d\mathbf{r}}, \quad (\text{I.12})$$

or for our surface parameterized by u and v

$$\kappa_n = \frac{Ldu^2 + 2Mdudv + Ndv^2}{Edu^2 + 2Fdudv + Gdv^2}. \quad (\text{I.13})$$

Defining $\lambda = dv/du$, we can write the curvature in the direction du/dv as [I.4]

$$\kappa = \frac{L + 2M\lambda + N\lambda^2}{E + 2F\lambda + G\lambda^2}. \quad (\text{I.14})$$

The extrema of κ are found by setting $d\kappa/d\lambda = 0$. Thus,

$$(E + 2F\lambda + G\lambda^2)(M + N\lambda) - (L + 2M\lambda + N\lambda^2)(F + G\lambda) = 0. \quad (\text{I.15})$$

Now

$$\begin{aligned} (E + 2F\lambda + G\lambda^2) &= (E + F\lambda) + \lambda(F + \lambda G), \\ (L + 2M\lambda + N\lambda^2) &= (L + M\lambda) + \lambda(M + \lambda N), \end{aligned} \quad (\text{I.16})$$

we can use (I.15) and (I.16) to rewrite (I.14) as

$$\kappa = \frac{L + M\lambda}{F + G\lambda} = \frac{L + M\lambda}{E + F\lambda}. \quad (\text{I.17})$$

Thus, κ must satisfy

$$\begin{aligned} (\kappa E - L)du + (\kappa F - M)dv &= 0, \\ (\kappa F - M)du + (\kappa G - N)dv &= 0. \end{aligned} \quad (\text{I.18})$$

Elimination of κ from (I.18) yields a quadratic equation for λ

$$(FN - GM)\lambda^2 + (EN - GL)\lambda + EM - FL = 0. \quad (\text{I.19})$$

This equation has real roots that define the directions of principal curvature. The roots are

$$\lambda_{1,2} = \frac{GL - EN}{2(FN - GM)} \pm \frac{\sqrt{(GL - EN)^2 + 4(FN - GM)(FL - EM)}}{2(FN - GM)}, \quad (\text{I.20})$$

and satisfy the condition that the directions λ_1 and λ_2 are orthogonal [I.2]

$$\begin{aligned} G\lambda_1\lambda_2 &= +F(\lambda_1 + \lambda_2) + E = \\ -\frac{1}{(FN - GM)}[G(EM - FL) - F(GL - EN) + E(FN - GM)] &= 0. \end{aligned} \quad (\text{I.21})$$

Since the principal curvature directions are orthogonal, it follows that $F = 0 = M$. The principal curvatures (I.18) are then

$$\kappa_1 = \frac{L}{E}, \quad \kappa_2 = \frac{N}{G}, \quad (\text{I.22})$$

and the mean curvature, $\bar{\kappa}$, is defined by

$$J = 2\bar{\kappa} = \frac{GL + EN}{H^2}. \quad (\text{I.22})$$

1.3 Formulation of the problem

We consider a liquid bridge held between coaxial equidimensional disks of radius R and subject to an axial gravity vector. The dependent variables have been made dimensionless using $(\gamma/|\Delta\rho g|)^{1/2}$ as a length scale and $(\gamma|\Delta\rho g|)^{1/2}$ as a pressure scale. here γ is the surface tension, g is the magnitude of the gravitational acceleration and $\Delta\rho$ is the difference between the density of bridge liquid and the bath liquid. A cylindrical coordinate system (r,θ,z) with its origin at the center of the lower disk and with z parallel to the bridge axis is employed (see section I.I). The bridge shape is then described in terms of its coordinates $(r(s),z(s))$ which are parameterized by the arclength s . The values of $r(s)$ and $z(s)$ depend on three parameters, the aspect ratio or slenderness, $\Lambda = L/2R$, the Bond number, $Bo = |\Delta\rho g|R^2/\gamma$, and the relative volume $V = V_0/\pi R^2 L$.

At the interface between liquid bridge and the surrounding bath liquid, equilibrium dictates that the pressure in the bridge liquid and the bath must be linearly increasing functions of z . Furthermore, the difference in pressure between the liquid within the bridge and the exterior liquid must be equal to the product of the surface tension and the curvature. In terms of our non-dimensional variables we have

$$p_1 = p_{01} - \rho_1^* z, \quad p_2 = p_{02} - \rho_2^* z,$$

where p_1 and p_2 denote the total pressure in the liquid bridge and the bath, respectively, and the ρ_i^* $i=1,2$ are the ratios of the bridge and bath densities to $\Delta\rho$. The reference pressures p_{01} and p_{02} are the liquid bridge and bath pressures evaluated at $z=0$. At each point on the liquid bridge surface the following equation must also be satisfied

$$p_{01} - p_{02} - \varepsilon z = -2\bar{H} \quad (I.23)$$

where \bar{H} is the dimensionless mean curvature and $\varepsilon = \text{sign}(\Delta\rho)$.

In order to express \bar{H} in terms of the variable describing the bridge shape we proceed as follows. First we consider the position vector $\mathbf{r}(s,\theta)$ to a point on the surface where

$$\mathbf{r}(s,\theta) = r(s) \mathbf{e}_r + z(s)\mathbf{e}_z, \quad (I.24)$$

where θ is the azimuthal variable and \mathbf{e}_r and \mathbf{e}_z are unit vectors parallel to the r and z coordinates, respectively. Taking the derivatives of \mathbf{r} with respect to the surface coordinates s and θ yields the quantities necessary to calculate the first and second order magnitudes E, L, N and G that are needed to compute the mean curvature form (I.22). They are

$$\begin{aligned} \mathbf{r}_1 &= r' \mathbf{e}_r + z' \mathbf{e}_z, \quad \mathbf{r}_\theta = -r \mathbf{e}_\theta, \\ \mathbf{r}_{11} &= r'' \mathbf{e}_r + z'' \mathbf{e}_z, \quad \mathbf{r}_{22} = -r \mathbf{e}_r, \end{aligned} \quad (I.25)$$

Now, we have from (I. 2), (I.3), (I.8), (I.10) and (I.25)

$$E = r'^2 + z'^2, \quad G = r^2, \quad (I.26)$$

$$\mathbf{n} = \frac{\mathbf{r}_1 \wedge \mathbf{r}_2}{\sqrt{EG}} = \frac{z' \mathbf{e}_r - r' \mathbf{e}_z}{(r'^2 + z'^2)^{1/2}},$$

and

$$L = \frac{r''z' - r'z''}{(r'^2 + z'^2)^{1/2}}, \quad N = \frac{-rz'}{(r'^2 + z'^2)^{1/2}}. \quad (I.27)$$

Finally, we obtain the mean curvature from (I.22)

$$2\bar{H} = - \frac{[z'(r'^2 + z'^2) + r(r'z'' - r''z')]}{r(r'^2 + z'^2)^{3/2}} = \frac{1}{r'} \left(\frac{rz'}{(r'^2 + z'^2)^{1/2}} \right)'. \quad (I.28)$$

Thus the equilibrium condition becomes

$$\frac{1}{r'} \left(\frac{rz'}{(r'^2 + z'^2)^{1/2}} \right)' = -C + \varepsilon z, \quad (I.29)$$

where

$$C = \frac{p_{01} - p_{02}}{\sqrt{\gamma|\Delta\rho|g}}. \quad (I.30)$$

Equation (I.30) can be further simplified by noting that the rates of change of r and z with s are related to the contact angle ϕ through

$$r' = \cos \phi, \quad z' = \sin \phi. \quad (I.31)$$

Differentiating (I.31) with respect to s and substituting (I.31) into (I.29) and we obtain the following coupled system of nonlinear ordinary differential equations

$$r''(s) = -z'(s)\phi'(s), \quad 0 < s < s^*, \quad (I.32)$$

$$z''(s) = r'(s)\phi'(s), \quad 0 < s < s^*, \quad (I.33)$$

$$\phi'(s) = C - \varepsilon z(s) - \frac{z'(s)}{r(s)}, \quad 0 < s < s^*. \quad (I.34)$$

The corresponding boundary conditions are

$$r(0) = \sqrt{Bo}, \quad (I.35)$$

$$r(s^*) = \sqrt{Bo}, \quad (I.36)$$

$$z(0) = 0, \quad (I.37)$$

$$z(s^*) = 2\Lambda\sqrt{\text{Bo}}. \quad (\text{I.38})$$

The constant C in (I.31) is determined from the constant volume constraint

$$V = (2\Lambda)^{-1} \text{Bo}^{-3/2} \int_0^{s^*} r(s)z(s)ds. \quad (\text{I.39})$$

Rather than treating the system as a boundary value problem, we follow an approach taken by Slobozhanin and Perales [I.4] and employ a shooting method. The boundary conditions (I.35) and (I.36) are replaced by the initial conditions

$$r'(0) = \cos \phi_1, \quad (\text{I.40})$$

$$z'(0) = \sin \phi_1, \quad (\text{I.41})$$

and equation (I.33) is integrated with

$$\phi(0) = \phi_1, \quad (\text{I.42})$$

as an initial condition. For each choice of ϕ_1 the system is solved using a Bulirsch-Stoer method [I.5]. The integration continues until z satisfies the condition (I.38) at some s^* . At this point the bridge radius and volume V are calculated. If (I.36) and (I.39) are not satisfied then C and ϕ_1 must be adjusted so that these conditions may be fulfilled at the next attempt. The new values of C and ϕ_1 are obtained using a Newton technique. The method we employ involves taking $r(s^*)$ and V as implicit functions of C and ϕ_1 . That is,

$$G_1(r^*, C, \phi_1) = r^* - F_1(C, \phi_1) = 0, \quad (\text{I.43})$$

$$G_2(V, C, \phi_1) = V - F_2(C, \phi_1) = 0. \quad (\text{I.44})$$

We use a subroutine called *hybrid1* developed at the Argonne National Laboratory as part of the MINPAK project calculate the Jacobians of the nonlinear functions G_1 and G_2 . The new values of C and ϕ_1 are then obtained through Newton's method, and equations (I.32)-(I.34) are solved again with the new C and ϕ_1 . The procedure is repeated until (I.36) and (I.39) are satisfied to within some specified tolerance. The quantity C is then rescaled by multiplication by $\sqrt{\text{Bo}}$ and is then used along with the computed value of ϕ_1 to calculate the dimensionless force F of section 3.

References for Appendix I

- [I.1] D. J. Struik, *Differential Geometry* (Addison-Wesley, 1961) p.74.
- [I.2] *ibid.* p.59.
- [I.3] *ibid.* p.80.
- [I.3] L. A. Slobozhanin and J.M. Perales, *Phys. Fluids A*, **5** (1993) 1305.
- [I.4] W.H. Press, Brian P. Flannery, S.A. Teukolsky and W.T. Vetterling, *Numerical Recipes* (Cambridge University Press, Cambridge, 1986) p.563.

J. Meseguer, M. A. González, and J. I. D. Alexander

Dynamic Stability of Long, Axisymmetric Liquid Bridges

NDB

This paper deals with the non-linear forced oscillations of axisymmetric long liquid bridges between equal disks. The dynamics of the liquid bridge has been analyzed by using a self-similar, one-dimensional model already used in similar problems. The influence of the dynamics on the static stability limits, as well as the main characteristics of the non-linear behaviour of long liquid bridges, have been studied within the range of validity of the mathematical model used here.

1 Introduction

In the last years isothermal liquid bridges have focused the attention of many investigators, with a large number of published papers on this topic (a review of the literature related to liquid bridges can be found in Sanz-Andres [1]). Because of the large number of parameters involved, the study of liquid bridges becomes a formidable task which extends in time from the early paper of Gillette and Dyson [2] to the late paper of Slobozhanin and Perales [3]. Most of these papers are only concerned with static stability limits. As far as we know only a few attempts have been made to analyze the influence of the dynamics of the liquid bridge, and these efforts have been centred more in the dynamics itself than in its influence on the stability limits (Meseguer [4], Rivas and Meseguer [5], Perales and Meseguer [6], Sanz and López-Diez [7], Zhang and Alexander [8], Langbein [9], Schulkes [10], among others).

In this paper the influence of the dynamics on the stability limits of liquid bridges is analyzed by using a simplified one-dimensional, self-similar model which, in spite of its simplicity, allows us to get some feeling on the dynamical behaviour of long liquid bridges. Associated with stability limits is the concept of stability margin, which has been defined as the difference between the energy of the stable equilibrium shape and of the unstable one for a given liquid bridge. The stability margin gives an estimate of the minimum energy which is needed to break a liquid bridge

through a given perturbation. Stability margins are discussed in sect. 2, whereas in sect. 3 the forced oscillations of long liquid bridges are analyzed, and stability diagrams for such kinds of perturbation are obtained.

2 Problem Formulation

The fluid configuration under consideration consists of an axisymmetric liquid bridge, with constant density ρ , kinematic viscosity ν and surface tension σ , held by capillary forces between two coaxial, solid disks of radius R which are a distance L apart, as sketched in fig. 1. The volume of liquid, V' , is assumed to be almost the volume of a cylinder of the same R and L , $V' \approx \pi R^2 L$, and it is also assumed that there is a small gravity field acting parallel to the liquid bridge axis. To describe the behaviour of such a fluid configuration the following dimensionless parameters are introduced: slenderness $\Lambda = L/(2R)$, dimensionless volume $V = V'/R^3$, Bond number $B = \rho g R^2/\sigma$, and viscosity parameter $C = \nu(\rho/(\sigma R))^{1/2}$. In addition to these parameters, it must be stated that all physical magnitudes used in the following have been made dimensionless by using R and $(\rho R^3/\sigma)^{1/2}$ as characteristic length and characteristic time, respectively.

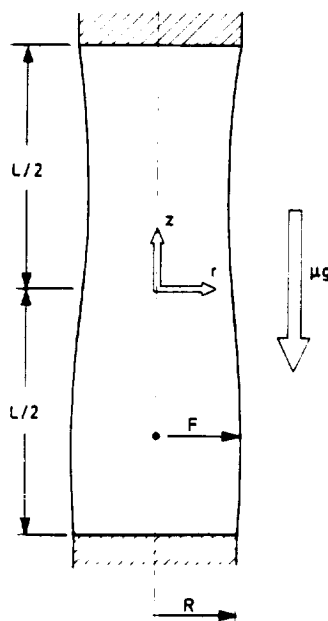


Fig. 1. Geometry and coordinate system for the liquid bridge problem

Mail address: Prof. J. Meseguer, M. A. González, Iamf, E.T.S.I. Aeronáuticos, Universidad Politécnica de Madrid, E-28040 Madrid, Spain; Dr. J. I. D. Alexander, Center for Microgravity and Materials Research (CMMR), The University of Alabama in Huntsville, Huntsville, AL 35899, USA.

Paper submitted: May 25, 1993.

Submission of final revised version: December 2, 1993.

Paper accepted: January 7, 1994.

It has been demonstrated in *Rivas and Meseguer* [5] that close to the static stability limit of cylindrical liquid bridges ($A \approx \pi$, $B \approx 0$, $V \approx 2\pi A$) there is a self-similar solution for the dynamics of the liquid bridge. These authors performed their analysis by using a one-dimensional model in which the axial velocity is assumed to be dependent on the axial coordinate z and the time t , but not on the radial coordinate r (such hypothesis has proved to be valid provided the slenderness is high enough, say $A > 1.5$, *Perales and Meseguer* [6]). Within the validity range of such analysis the variation with time of the interface deformation is given by the Duffing equation

$$\ddot{x}_{nn} + \gamma \dot{x}_{nn} - m x - x^3 = \tilde{\beta} \quad (1)$$

where

$$x = \frac{1}{4} A \left(\frac{1}{3} \delta \right)^{-1/2}, \quad \theta = \frac{2}{5} t (2\delta)^{1/2}, \quad (2)$$

$$\gamma = \frac{5}{2} C (2\delta)^{-1/2}, \quad \tilde{\beta} = \frac{1}{2} B \left(\frac{1}{3} \delta \right)^{-1/2},$$

are the self-similar variables and parameters. In these last expressions A is the amplitude of the interface deformation, which in this model varies as $S(z, t) = 1 + A(t) \sin(\pi z)/A$ (formally A measures the deformation of a magnitude proportional to the liquid bridge cross-section, $S = F^2$), whereas δ stands for a reduced slenderness which includes volume effects:

$$-m\delta = 1 - \frac{A}{\pi} + \frac{1}{2} \left(\frac{V}{2\pi A} - 1 \right),$$

where δ is positive and m takes account for the sign ($m = \pm 1$); t is the dimensionless time and the parameters C and B have been already defined.

To simplify the explanation, let us denote the self-similar variables and parameters involved in the problem, as defined by expressions (2), with labels indicating their main physical meaning, so that in the following we refer to x , θ , γ , and $\tilde{\beta}$ as deformation of the liquid bridge interface, time, viscosity, and Bond number, respectively. Let us also assume that gravity oscillates around some mean value, in such a way that in self-similar variables the time variation of the Bond number can be written as $\tilde{\beta} = \beta + b \cos(\Omega\theta)$, where Ω stands for the self-similar frequency of the imposed perturbation. In such a case eq. (1) would be

$$\ddot{x}_{nn} + \gamma \dot{x}_{nn} - m x - x^3 = \beta + b \cos(\Omega\theta), \quad (3)$$

which allows one to analyze, within the validity range of this model, both the static stability margin and the forced non-linear response of the liquid bridge.

Static stability margin results from eq. (3) taking $b = 0$. The potential energy of the liquid bridge, which accounts for both gravity field and surface energies, in self-similar variables will be

$$\tilde{\xi} = -\frac{1}{2} m x^2 - \frac{1}{4} x^4 - \beta x, \quad (4)$$

where $\tilde{\xi}$ is related to dimensionless energy (made dimensionless with σR^2) through the expression

$$\tilde{\xi} = \frac{16}{3} (\pi\delta)^{-2} (E - E_0) \quad (5)$$

E_0 accounting for all terms contributing to energy which do not depend on the interface deformation. Equilibrium shapes are given by

$$\frac{d\tilde{\xi}}{dx} = -mx - x^3 - \beta = 0. \quad (6)$$

Eq. (6) has one real root if $m = +1$, which is unstable ($d^2\tilde{\xi}/dx^2 < 0$), and three real roots, $x_1 > x_2 > x_3$, in the case $m = -1$. From these, the two extreme roots, x_1 and x_3 , correspond to unstable equilibrium shapes, whereas the central one represents a stable configuration. Thus, within this approximation the stability margin will be the difference between the energy of the unstable equilibrium shapes and of the stable one, $\Delta\tilde{\xi} = \tilde{\xi}_{\text{unstable}} - \tilde{\xi}_{\text{stable}}$. This behaviour is summarized in fig. 2, where the variation of the roots x_1 , x_2 , and x_3 with β as well as the stability margins $\Delta\tilde{\xi}_1 = \tilde{\xi}(x_1) - \tilde{\xi}(x_2)$ and $\Delta\tilde{\xi}_3 = \tilde{\xi}(x_3) - \tilde{\xi}(x_2)$, are shown. Obviously, the stability margin is defined by the smaller of such values, $\Delta\tilde{\xi}_1$ in our case, which in the following will be denoted as $\Delta\tilde{\xi}$. According to eq. (5), in dimensionless variables the stability margin is given by $\Delta E = \frac{1}{16} \pi^2 \Delta\tilde{\xi} \delta^2$, that is, the stability margin is proportional to the square of the distance to the stability limit (such stability limit being $\delta = 0$), the proportionality constant, $\Delta\tilde{\xi}$, being smaller as the Bond number increases. This factor, hence the stability margin, becomes zero when $\beta = 2\sqrt{3}/9$, which represents, when dimensionless variables are used, the variation with

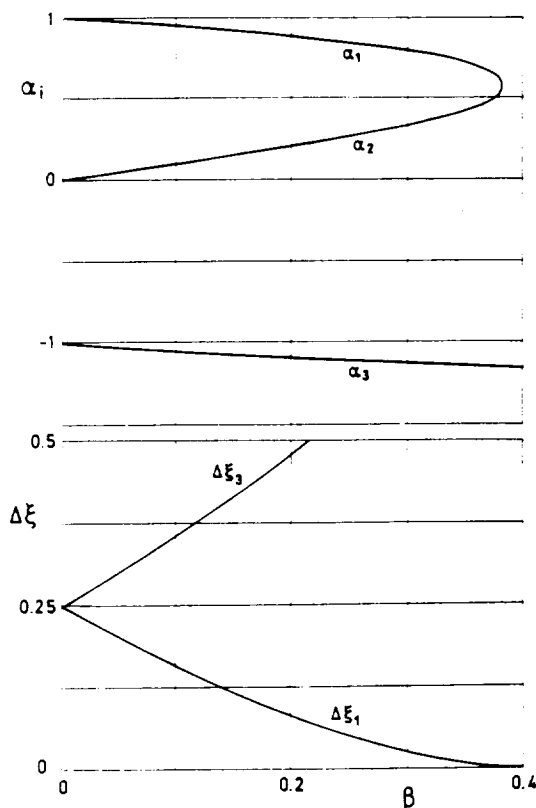


Fig. 2. Variation with the Bond number, β , of the roots, x_i , of eq. (6), which define the equilibrium shapes of a slender liquid bridge, and variation with β of the difference, $\Delta\tilde{\xi}_i$, between the energy of each one of the unstable equilibrium shapes and of the stable one

Bond number of the stability limit of almost cylindrical liquid bridges, $B = \frac{4}{3}\delta^{3/2}$, already calculated by Vega and Perales [11].

3 Dynamic Stability

The stability margin or safety margin represents a limit to the minimum energy needed to break the liquid bridge. That means that, for a given perturbation, the response of the liquid bridge will depend on the energy of the perturbation; the liquid bridge will remain stable if the energy is smaller than the corresponding stability margin and it could be unstable if such energy becomes bigger. Of course in this last case the evolution of the liquid bridge depends on how the perturbation is imposed and on how such energy is dissipated because of viscosity. To fix our ideas let us consider the forced oscillation of the liquid bridge in gravitational conditions ($\beta = 0$, $b \neq 0$). In that case $x_2 = 0$ and $x_1 = -x_3 = 1$, so the $\Delta\xi = \frac{1}{4}$. The time variation of the interface is now defined by the expression

$$x_{\theta\theta} + \gamma x_{\theta} + x - x^3 = b \cos(\Omega\theta + \varphi), \quad (7)$$

which, assuming steady oscillations are reached, can be integrated in a first approximation [12] obtaining $x = a \cos(\Omega\theta)$, where a is related to viscosity, γ , to the amplitude of the perturbation, b , and to the frequency of the perturbation, Ω , through the equation

$$a^2 \left(1 - \Omega^2 - \frac{3}{4} a^2 \right)^2 + \gamma^2 \Omega^2 a^2 = b^2. \quad (8)$$

Within this rough approximation (to write down eq. (8) a term in $a^3 \cos(3\Omega\theta)$ has been neglected) the oscillation of the liquid bridge can be easily visualized by plotting the liquid bridge evolution in the phase space (deformation-velocity-energy diagram), as shown in fig. 3. Note that,

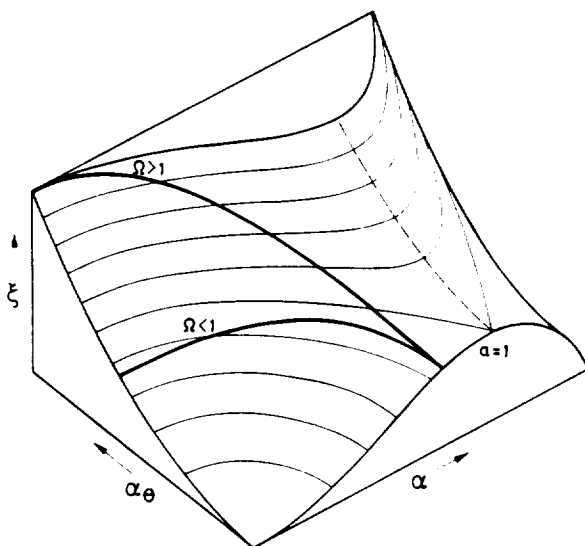


Fig. 3. Phase space (deformation of the interface, α , velocity, α_{θ} , and energy, ξ) of the forced oscillations of a liquid bridge according to the simplified model given by eq. (8). There are two evolutions represented in this plot, $\Omega > 1$ and $\Omega < 1$, where Ω stands for the pulsation of the forcing action

since we are considering an evolution, kinetic energy must be also taken into account, so that at every point of the phase space the energy will be the sum of the potential energy plus the kinetic energy:

$$\xi = \frac{1}{2} \dot{x}^2 - \frac{1}{4} x^4 + \frac{1}{2} x_{\theta}^2. \quad (9)$$

Two different oscillations of the liquid bridge, with amplitude $a < 1$, have been also represented in fig. 3, one corresponding to $\Omega < 1$ and the other corresponding to $\Omega > 1$. Note that, for the movement under consideration, the energy of the liquid bridge, hence the energy of the perturbation, can be greater than that corresponding to the stability margin ($\Delta\xi = \frac{1}{4}$) and the configuration remain stable, as it happens in the $\Omega > 1$ case.

According to the plot of fig. 3, the liquid bridge will be unstable when $a = 1$, and, in that case, eq. (8) gives us the relationship between the viscosity γ and the parameters defining the perturbation

$$\gamma^2 = \Omega^{-2} \left[b^2 - \left(\frac{1}{4} - \Omega^2 \right)^2 \right]. \quad (10)$$

Once b and Ω are fixed, the liquid bridge evolution will be stable if the viscosity of the liquid is greater than the value resulting from eq. (10), otherwise it will be unstable. This behaviour is summarized in fig. 4, which has been plotted by using eq. (10). For a given viscosity γ and frequency Ω the evolution will be unstable if the point representing this evolution lies on the left of the corresponding b -curve, and stable if the point lies on the right.

Of course, this description of the phenomenon must be regarded as qualitative only. The results obtained are based on the assumption that the response of the liquid bridge is co-sinusoidal ($x = a \cos(\Omega\theta)$) which, as already stated, is only a rough approximation to the solution of eq. (7).

To get more precise results, eq. (7) has been numerically integrated by using a fourth-order Runge-Kutta method and the trajectories in the phase-plane obtained. Depending on the values of the parameters involved (γ , b , and Ω) and the initial conditions these trajectories can be closed curves (the deformation of the liquid bridge interface, α , remains bounded no matter what the value of θ is) or the deformation continuously grows with time. The first case means that the liquid bridge is stable for the imposed perturbation, whereas in the second case the fluid configuration becomes unstable. The border between the two cases being the dynamic stability limit for the perturbation under consideration. When forced oscillations are considered the stability limit depends, as already stated, on the nature of the perturbation imposed and on the initial conditions. To avoid the influence of the starting transient, calculations have been performed as follows: first of all a set of values of the parameters γ , b , and Ω for which the liquid bridge evolution is clearly stable is chosen (this is achieved by selecting a high value of viscosity γ). Once a steady oscillation for the selected set of values of the parameters is reached, the value of one of the parameters is slightly changed (in our case the value of γ is slightly reduced at the beginning of a cycle); in this way initial conditions for the second set of values of the parameters are extremely close

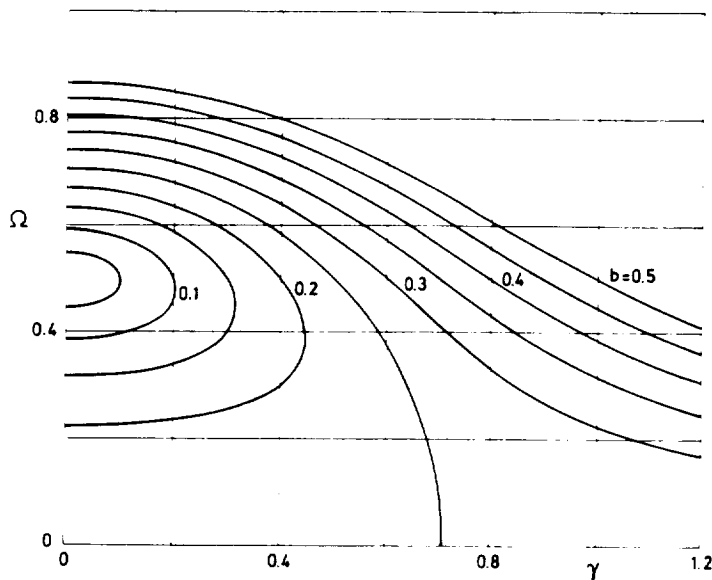


Fig. 4. Stability diagram in self-similar variables as given by eq. (10). Points at the left of each curve $b = \text{const.}$ are unstable for this value of b , whereas those lying at the right are stable

to that corresponding to a steady oscillation and transient effects due to initial conditions can be made negligible.

The results obtained are shown in fig. 5. Also in this plot each one of the curves $b = \text{const.}$ represents the corresponding stability limit. Points at the right of a given curve represent stable evolutions (high values of the viscosity, γ) whereas those at the left side region (low values of γ) correspond to unstable evolutions. Note that once γ and b are fixed there is one or even two sets of values of Ω for which the liquid bridge evolution becomes unstable.

The response of the liquid bridge, defined as x_m/b where x_m stands for the maximum value of x in each cycle, is shown in fig. 6 for different values of b .

To get an idea of the importance of initial conditions on the response of the liquid bridge eq. (7) has been integrated

again with initial conditions $x = 0, \dot{x}_0 = 0$. The stability limit corresponding to $b = 0.5$ obtained by using this initial condition (curve labelled 2 in fig. 7) is compared with the calculated taking "steady" initial conditions (curve 1). Note that the influence of initial conditions becomes negligible when Ω is small enough, but that differences can be remarkable as the value of Ω increases.

Finally, it must be said that the Duffing equation, here used to analyze the non-linear forced oscillation of long liquid bridges, is a typical example of a non-linear oscillator in which chaos phenomena appear [13]. Such chaotic behaviour has been detected in our calculation, it clearly appears when both Ω and γ are small, although no attempts have been made to perform a deep analysis of such behaviour, which is out of the scope of this paper.

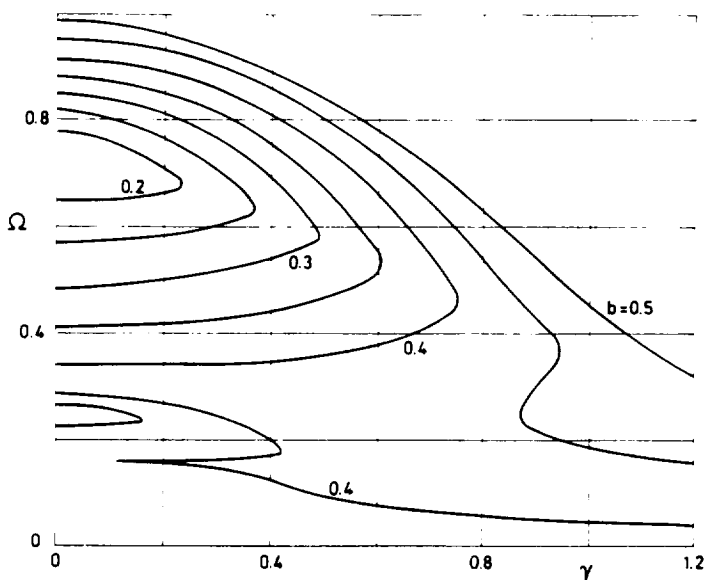


Fig. 5. Stability diagram in self-similar variables obtained by numerical integration of eq. (3). Points at the left of each curve $b = \text{const.}$ are unstable for this value of b , whereas those lying at the right are stable

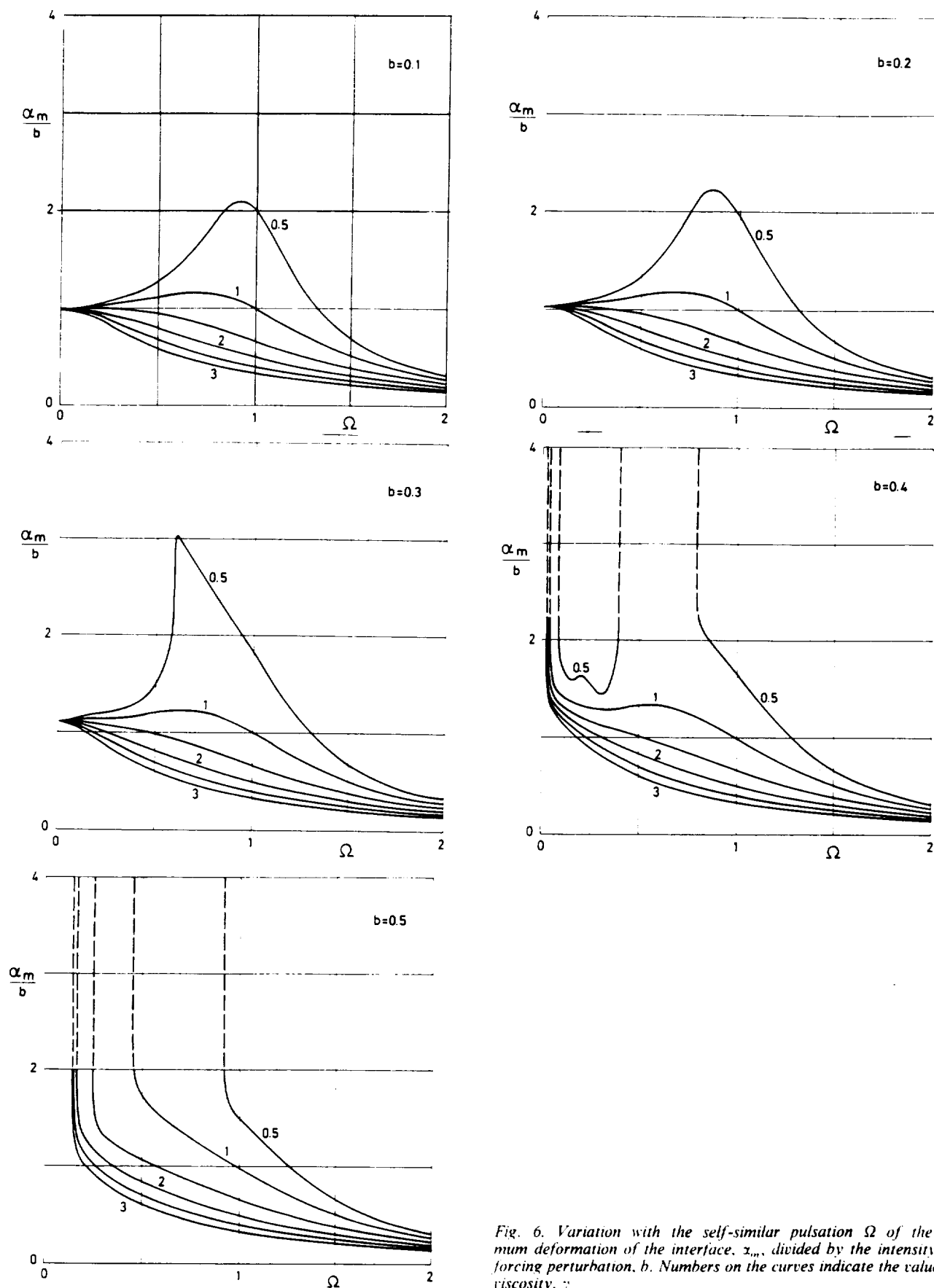


Fig. 6. Variation with the self-similar pulsation Ω of the maximum deformation of the interface, α_m , divided by the intensity of the forcing perturbation, b . Numbers on the curves indicate the value of the viscosity, γ .

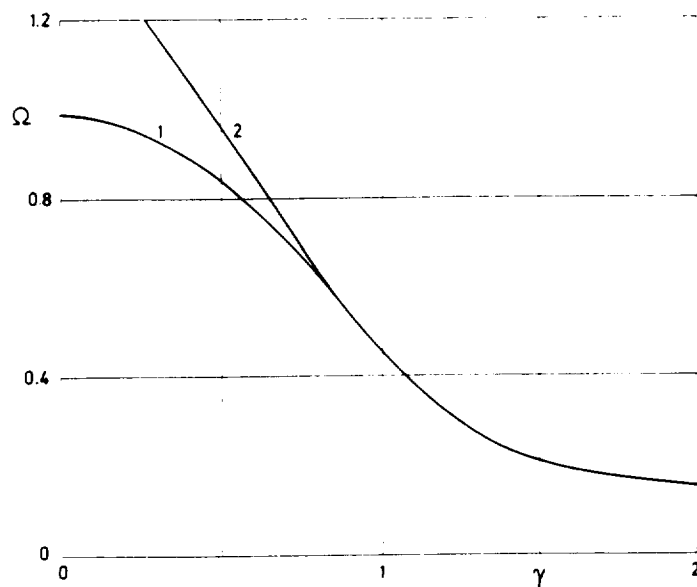


Fig. 7. Influence of the initial conditions on the stability diagram. Curves 1 and 2 have been obtained under different initial conditions as explained in the text

Acknowledgments

This work has been supported by the Spanish Comisión Interministerial de Ciencia y Tecnología (CICYT) and is part of a more general endeavour for the study of fluid physics and materials processing under microgravity (Project No. ESP92-0001-CP).

References

- 1 Sanz-Andres, A.: Static and Dynamic Response of Liquid Bridges; in *Microgravity Fluid Mechanics*, H. J. Rath (ed.), Springer-Verlag, Berlin, p. 3 (1992)
- 2 Gillette, R. D., Dyson, R. C.: Stability of Fluid Interfaces of Revolution Between Equal Solid Circular Plates. *Chem. Eng. J.*, vol. 2, p. 44 (1971)
- 3 Slobozhanin, L. A., Perales, J. M.: Stability of Liquid Bridges Between Equal Disks in an Axial Gravity Field. *Phys. Fluids A*, vol. 5, p. 1305 (1993)
- 4 Meseguer, J.: The Breaking of Axisymmetric Slender Liquid Bridges. *J. Fluid Mech.*, vol. 130, p. 123 (1983)
- 5 Rivas, D., Meseguer, J.: One-dimensional, Self-similar Solution of the Dynamics of Axisymmetric Slender Liquid Bridges. *J. Fluid Mech.*, vol. 138, p. 417 (1984)
- 6 Perales, J. M., Meseguer, J.: Theoretical and Experimental Study of the Vibration of Axisymmetric Viscous Liquid Bridges. *Phys. Fluids A*, vol. 4, p. 1110 (1992)
- 7 Sanz, A., López-Diez, J.: Non-axisymmetric Oscillations of Liquid Bridges. *J. Fluid Mech.*, vol. 205, p. 503 (1989)
- 8 Zhang, Y., Alexander, J. I. D.: Sensitivity of Liquid Bridges Subject to Axial Residual Acceleration. *Phys. Fluids A*, vol. 2, p. 1966 (1990)
- 9 Langbein, D.: Oscillations of Finite Liquid Columns. *Microgravity Sci. Technol.*, vol. 5, p. 73 (1992)
- 10 Schulkes, R. M. S. M.: Non Linear Liquid Bridge Dynamics. ESA SP-333, vol. 1, p. 61, ESA Publ. Div., ESTEC, Noordwijk (1992)
- 11 Vega, J. M., Perales, J. M.: Almost Cylindrical Isorotating Liquid Bridges for Small Bond Numbers. ESA SP-191, p. 247, ESA Publ. Div., ESTEC, Noordwijk (1992)
- 12 Stoker, J. J.: *Nonlinear Vibrations*, Vol. II, Interscience (1966)
- 13 Thompson, J. M. T., Steward, M. B.: *Nonlinear Dynamics and Chaos*, John Wiley & Sons Ltd., Chichester (1988)